Structural Novelty Detection Based on Laplace Asymptotic Expansion of the Bhattacharyya Distance of Transmissibility Function and Bayesian Resampling Scheme

Lin-Feng Mei[1], Wang-Ji Yan[1,2]*, Ka-Veng Yuen[1,2]*, Beer Michael[3,4,5]

[1]State Key Laboratory of Internet of Things for Smart City and Department of Civil and Environmental Engineering, University of Macau, China

[2]Guangdong–Hong Kong-Macau Joint Laboratory for Smart Cities, University of Macau, China

[3]Leibniz Universität Hannover, Institute for Risk and Reliability, Hannover, Germany

[4]University of Liverpool, Institute for Risk and Uncertainty, Peach Street, L69 7ZF Liverpool, United Kingdom

[5]Tongji University, International Joint Research Center for Engineering Reliability and Stochastic Mechanics, Shanghai 200092, China

Abstract: As an output-to-output dynamical representation of engineering structures, the transmissibility function (TF) has been widely reported to be a damage-sensitive but excitation-insensitive damage feature. However, most TF-based novelty detection approaches fail to accommodate various uncertainties with a proper probabilistic model. Making full use of the complex Gaussian ratio probabilistic model of raw scalar TFs, a data-driven structural novelty detection technology is proposed by integrating the closed-form approximation of the Bhattacharyya distance of TFs and the Bayesian resampling scheme. A closed-form approximation of the Bhattacharyya distance is efficiently derived by applying the Laplace method of asymptotic expansion to provide a probabilistic metric of the dissimilarity between distributions of TFs under different states without resorting to time-consuming numerical integration. A Bayesian resampling scheme is adopted to accommodate the variability of the statistical parameters involved in the probabilistic model of TFs. Based on the Laplace asymptotic expansion of the Bhattacharyya distance and Bayesian resampling scheme, two state discrimination techniques including Gaussian mixture model (GMM) clustering method and threshold method are utilized to detect the existence of damage. Two case studies, including a laboratory model test as well as a field test of a bridge, are carried out to verify the accuracy and efficiency of the proposed algorithm. The results demonstrate that, compared with the Mahalanobis distance-based method with the implicit assumption of Gaussian distribution for TFs, the Bhattacharyya distance-driven algorithm can achieve better performance and robustness due to properly considering the deviations in TFs not following the Gaussian distribution.

Keywords: Transmissibility; Novelty detection; Bhattacharyya distance; Bayesian inference; Clustering.

*Corresponding author.
E-mail address: wangjiyan@um.edu.mo (W.J. Yan); kvyuen@um.edu.mo (K.V. Yuen); yc17409@connect.um.edu.mo (L.F. Mei); beerirz.uni-hannover.de (M. Beer)

1. Introduction

The service life of engineering structures decreases due to complex environmental and operational conditions, which may lead to unanticipated structural failure and cause serious property loss and casualties. As a result, much effort has been devoted to preventing disaster. Structural health monitoring (SHM), which uses periodically sampled response measurements to monitor changes of engineering structures, is viewed as one of the most cost-effective methods [1].

Among different types of SHM systems, NDE-based methods and vibration-based techniques have attracted increasing attention over the past few decades [1, 2]. The NDE techniques such as acoustic or ultrasonic methods offer high sensitivity to small structural changes and their implementation normally involves high frequency excitation and actuator to achieve the sensitivity [2]. Though NDE approaches pose significant potential and have shown full-fledged applications, vibration-based methods are still required for many cases due to their unique advantages. NDE techniques are often restricted to damage detection on or near the surface of the structure, which limits their application to small-scale structures [3-5]. Therefore, NDE methods are capable for ‘‘local’’ inspection while structural damage identification through changes in vibration-based health index provide “global’’ evaluation for the structural state [6], which makes them a better choice for large-scale infrastructures. Unfortunately, structural dynamic properties have often been reported to be insensitive to damage [7], which motivates researchers to find new vibration-based features more sensitive to damage. The transmissibility function (TF) has been widely viewed as a good candidate [8, 9] due to the following advantages: (i) Compared with dynamic properties, TF is more sensitive to structural damage;

(ii) TF-based novelty detection suits the situation in which the excitation is inaccessible, and it is more robust to natural excitation; (iii) Neither modal identification nor a numeric model of the structure is required for TF-based novelty detection [10]; (iv) By making full use of a wide frequency band, TF contains more information in addition to modal properties.

TF was first proposed as a SHM feature by Chen et al. [11]. Since then, a considerable amount of research has been conducted on TF-based novelty detection. A major milestone was reached when a research group at NASA proposed the use of the integral over a frequency band of the difference between two TFs corresponding to the control (healthy) and the possibly damaged states as a damage indicator for structural anomaly detection [12]. This method has since been adopted and further developed in [13, 14]. Cheng and Cigada [15] proposed an analytical perspective of TFs between two consecutive masses based on the motion equation of the multiple-degree-of-freedom (MDOF) mass-spring-damper model, the feasibility of which for damage identification has been validated via simulation and experimental studies. Farrar and Worden [1, 16] pointed out that a data-driven approach based statistical pattern recognition was the best framework for state discrimination in SHM. Taking this viewpoint, many novel data-driven novelty detection algorithms have been proposed and applied to SHM [17]. Worden and his colleagues [18, 19] proposed substantial TF-based indices through a combination of pattern recognition with machine learning techniques for novelty detection to diagnose damage. The feasibility and performance were validated using dynamic responses of various engineering structures in [20]. Clustering techniques have been widely reported to be good candidates for novelty detection under unknown sources of variability [21]. Zhou et al. [22] adopted clustering and Mahalanobis distance to distinguish damaged patterns from undamaged ones.

Despite excellent achievements in TF-based novelty detection, most existing methods are incapable of modelling uncertainties stemming from the nature of stochastic vibration, quantization and estimation error, noise originating from the acquisition configuration, the variability of environmental and operational conditions, and so on [7]. A pioneering work on accommodating the uncertainties of TF in novelty detection was carried out by Mao and Todd [23, 24], in which a statistical model quantifying the uncertainty of the magnitude of TFs was established based on power spectral density (PSD). The probability density function (PDF) was subsequently employed to examine statistical damage significance under a certain confidence level. Poulimenos and Sakellariou [25] proposed a cross spectral density (CSD) based uncertainty quantification method by adopting statistical hypothesis testing procedures with the likelihood ratio (LR) test for novelty detection.

In this work, a data-driven novelty detection technology is developed by accommodating the variability of frequency responses based on the theoretical findings of the probability distribution of raw TFs [26, 27]. The underlying premise of this study is the hypothesis that structural damage can be detected by adopting a damage indicator capable of accurately identifying the difference between TFs under two states. The Bhattacharyya distance (D_B) in statistics is a probability distance, and it is one of the most widely adopted metrics of the similarity between two probability distributions. Though the potential of D_B for feature extraction and selection has been demonstrated in many studies [28, 29], it has rarely been applied in novelty detection. In this study, D_B is used to measure the difference between two probability distributions of TFs under the healthy state (baseline condition) and the possibly damaged state. An efficient algorithm based on the Laplace asymptotic expansion is proposed to calculate the closed-form approximation of D_B between two PDFs of TFs. Based on the analytical solution of D_B, a damage indicator is proposed to measure the structural condition. In addition, to properly accommodate the variability of model parameters of the probability model of TFs stemming from multiple uncertainties, a Bayesian inference-based resampling method is proposed to enhance the robustness. Two state discrimination methods, namely Gaussian mixture model (GMM) clustering method and threshold method, are utilized to detect the existence of damage. Two case studies are adopted to validate the feasibility and efficiency of this methodology.

A schematic view of the new method proposed in this study is shown in Fig. 1. In Section 2, the Bhattacharyya Distance (D_B) between PDFs of TFs under different structural states is adopted to indicate the occurrence of damage. Meanwhile, a closed-form approximation of D_B is proposed based on Laplace asymptotic expansion to reduce the computational cost of numerical integration. Then in Section 3, a damage indicator is constructed using the approximated D_B over a specific frequency band, and two methods including a GMM clustering method as well as a threshold value are adopted for state discrimination in combination with a Bayesian resampling scheme. Section 4 outlines the procedures of the structural novelty detection method. Two case studies including a laboratory experiment and a field test are used to verify the feasibility and efficiency of the proposed method in Section 5, while conclusions are drawn in Section 6.

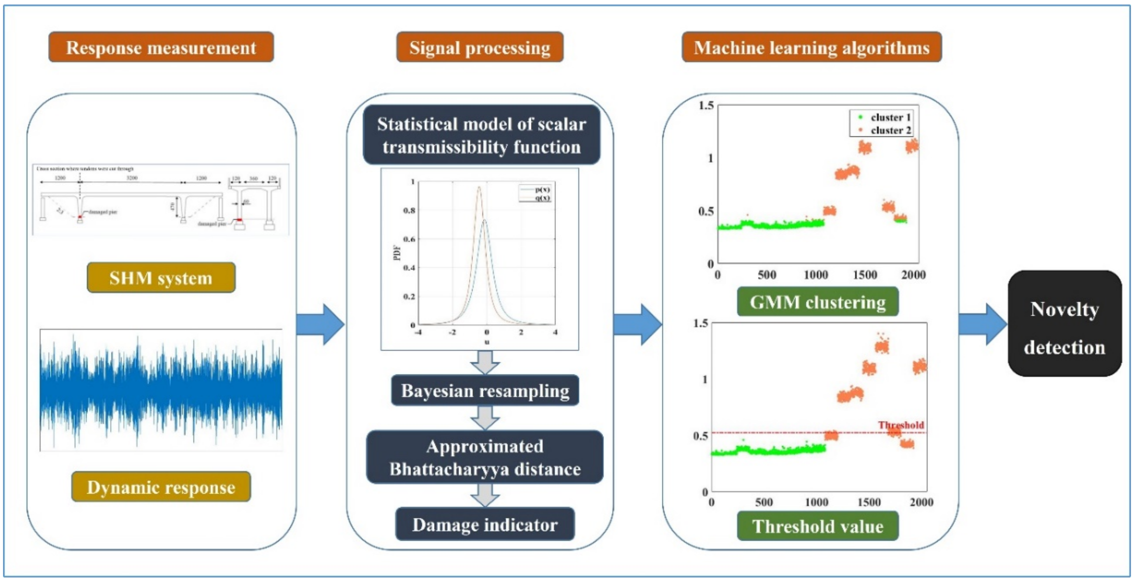

Figure 1. Schematic view of the methodology proposed in this study.

2. Closed-Form Approximation of Bhattacharyya Distance between TFs

2.1 Bhattacharyya distance

Bhattacharyya distance is a probabilistic metric that measures the difference between two probability distributions [30], and it has been widely applied in stochastic model updating as an uncertainty quantification (UQ) metric. By comparing the performance of the traditional Euclidian distance and the Bhattacharyya distance, it has been demonstrated that D_B could capture a higher level of statistical information from the investigating variables and is more comprehensive for dealing with uncertainty [31, 32]. For two probability distributions p and q over the same domain $\mathbf{\Theta}$, the Bhattacharyya distance is defined as:

$$D_B\left(p,q\right) = -\ln\left(BC\left(p,q\right)\right) \qquad (1)$$

where $BC(p,q)$ refers to the Bhattacharyya coefficient. For discrete and continuous probability distributions, the Bhattacharyya coefficient can be expressed in the continuous and discrete forms:

$$BC(p,q)=\sum_{x\in\Theta}\sqrt{p(x)q(x)} \tag{2a}$$

$$BC(p,q)=\int\sqrt{p(x)q(x)}dx \tag{2b}$$

2.2 Probabilistic model of TF

Consider a set of dynamic responses in time domain $\boldsymbol{y}(t)=\left\{y_1(t),y_2(t),\ldots,y_{n_o}(t)\right\}$ for n_o degree-of-freedoms (DOFs) of a linear system under a stationary excitation. The frequency domain responses of $\boldsymbol{y}(t)$ is denoted by $\boldsymbol{Y}_k=\boldsymbol{Y}_k^{\Re}+\mathrm{i}\boldsymbol{Y}_k^{\Im}$. $\boldsymbol{Y}_k^{\Re}$ and $\boldsymbol{Y}_k^{\Im}$ refer to the real and imaginary parts of $\boldsymbol{Y}_k$, respectively. It is worth noting that all "k" in the subscript or the superscript denote the frequency line ω_k in this work. The scalar TF is defined as $T_{ij}^k=\dfrac{Y_{i,k}}{Y_{j,k}}$, where $Y_{i,k}$ and $Y_{j,k}$ denote the responses corresponding to the i th and j th DOF. For an output vector $\boldsymbol{Y}_k=\left\{Y_{j,k},Y_{i,k}\right\}^T$, it has been proved that the mean of $\boldsymbol{Y}_k$ is approximately zero and its covariance matrix equals the expected value of the PSD matrix at the same frequency line $\mathbf{S}_k$ [33, 34]:

$$\boldsymbol{\Sigma}_{ij}^{\ k}=\mathbf{S}_k=\begin{bmatrix}\left(\sigma_i^{\ k}\right)^2 & \rho_{ij}^{\ k}\sigma_i^{\ k}\sigma_j^{\ k}\\ \rho_{ij}^{\ k*}\sigma_i^{\ k}\sigma_j^{\ k} & \left(\sigma_j^{\ k}\right)^2\end{bmatrix} \tag{3}$$

where $\sigma_i^{\ k}$ and $\sigma_j^{\ k}$ denote the variances of $Y_{i,k}$ and $Y_{j,k}$, respectively; $\rho_{ij}^{\ k}$ denotes the complex correlation coefficient between $Y_{i,k}$ and $Y_{j,k}$, and is given by $\rho_{ij}^{\ k}=\rho_{ij}^{\ k,\Re}+\mathrm{i}\rho_{ij}^{\ k,\Im}$, where $\rho_{ij}^{\ k,\Re}$ and $\rho_{ij}^{\ k,\Im}$ refer to the real and imaginary parts of $\rho_{ij}^{\ k}$, respectively. According to Yan et al. [26, 35], the TF follows a circularly-symmetric complex Gaussian ratio distribution with the PDF shown as follows:

$$P_U\left(\boldsymbol{u}_{ij}{}^k\right)=\frac{1}{\pi\left|\det\left(\boldsymbol{\Sigma}\right)\right|\left[\left(\boldsymbol{u}_{ij}{}^k\right)^T\left(\boldsymbol{\Sigma}\right)^{-1}\left(\boldsymbol{u}_{ij}{}^k\right)\right]^2} \tag{4}$$

where $\boldsymbol{u}_{ij}{}^k=\left\{1,u_{ij}^k\right\}^T$ and u_{ij}^k denotes the value of transmissibility between $Y_{j,k}$ and $Y_{i,k}$. The marginal PDF of the real and the imaginary parts of the TF ($u_{ij}^{k,\Re}$ and $u_{ij}^{k,\Im}$) can be derived [26]:

$$p\left(u_{ij}{}^{k,\Re}\right)=\frac{\left(1-\left|\rho_{ij}{}^k\right|^2\right)\left(\sigma_j{}^k\right)^4\left(\sigma_i{}^k\right)^2}{2\sqrt{\left\{-2\left(\sigma_j{}^k\right)^3\sigma_i{}^k\rho_{ij}{}^{k,\Re}u_{ij}{}^{k,\Re}+\left(\sigma_j{}^k\right)^4\left(u_{ij}{}^{k,\Re}\right)^2+\left(\sigma_j{}^k\right)^2\left(\sigma_i{}^k\right)^2\left[1-\left(\rho_{ij}{}^{k,\Im}\right)^2\right]\right\}^3}} \tag{5a}$$

$$p\left(u_{ij}{}^{k,\Im}\right)=\frac{\left(1-\left|\rho_{ij}{}^k\right|^2\right)\left(\sigma_j{}^k\right)^4\left(\sigma_i{}^k\right)^2}{2\sqrt{\left\{2\left(\sigma_j{}^k\right)^3\sigma_i{}^k\rho_{ij}{}^{k,\Im}u_{ij}{}^{k,\Im}+\left(\sigma_j{}^k\right)^4\left(u_{ij}{}^{k,\Im}\right)^2+\left(\sigma_j{}^k\right)^2\left(\sigma_i{}^k\right)^2\left[1-\left(\rho_{ij}{}^{k,\Re}\right)^2\right]\right\}^3}} \tag{5b}$$

Eq. (5) will be used to compute Bhattacharyya distance with a view towards novelty detection.

2.3 Bhattacharyya distance between TFs under two structural states

As previously mentioned, the occurrence of damage will change TFs, and such alteration could be captured via D_B between TFs under the healthy state and the possibly damaged state for novelty detection. For the healthy state, the PDFs of the real and imaginary parts of TFs between two arbitrary responses, $p\left(u_{ij}^{k,\Re}\right)$ and $p\left(u_{ij}^{k,\Im}\right)$, can be calculated using Eq. (5). To avoid confusion, the real and imaginary parts under the possibly damaged state are denoted by $p^d\left(u_{ij}^{k,\Re}\right)$ and $p^d\left(u_{ij}^{k,\Im}\right)$, and the covariance matrix of the Fast Fourier Transform (FFT) coefficients $\left\{Y_{j,k}^d,Y_{i,k}^d\right\}$ is expressed as:

$$\tilde{\boldsymbol{\Sigma}}=\begin{bmatrix}\left(\tilde{\sigma}_j{}^k\right)^2 & \tilde{\rho}_{ij}{}^k\tilde{\sigma}_j{}^k\tilde{\sigma}_i{}^k\\ \tilde{\rho}_{ij}{}^{k*}\tilde{\sigma}_j{}^k\tilde{\sigma}_i{}^k & \left(\tilde{\sigma}_i{}^k\right)^2\end{bmatrix} \tag{6}$$

Based on Eq. (5), $p^d\left(u_{ij}^{k,\Re}\right)$ and $p^d\left(u_{ij}^{k,\Im}\right)$ can be expressed as Eq. (7):

$$p^{d}\left(u_{ij}^{k,\mathfrak{R}}\right)=\frac{\left(1-\left|\tilde{p}_{ij}^{k}\right|^{2}\right)\left(\tilde{\sigma}_{j}^{k}\right)^{4}\left(\tilde{\sigma}_{i}^{k}\right)^{2}}{2\sqrt{\left\{-2\left(\tilde{\sigma}_{j}^{k}\right)^{3}\tilde{\sigma}_{i}^{k}\tilde{p}_{ij}^{k,\mathfrak{R}}u_{ij}^{k,\mathfrak{R}}+\left(\tilde{\sigma}_{j}^{k}\right)^{4}\left(u_{ij}^{k,\mathfrak{R}}\right)^{2}+\left(\tilde{\sigma}_{j}^{k}\right)^{2}\left(\tilde{\sigma}_{i}^{k}\right)^{2}\left[1-\left(\tilde{p}_{ij}^{k,\mathfrak{I}}\right)^{2}\right]\right\}^{3}}} \tag{7a}$$

$$p^{d}\left(u_{ij}^{k,\mathfrak{I}}\right)=\frac{\left(1-\left|\tilde{p}_{ij}^{k}\right|^{2}\right)\left(\tilde{\sigma}_{j}^{k}\right)^{4}\left(\tilde{\sigma}_{i}^{k}\right)^{2}}{2\sqrt{\left\{2\left(\tilde{\sigma}_{j}^{k}\right)^{3}\tilde{\sigma}_{i}^{k}\tilde{p}_{ij}^{k,\mathfrak{I}}u_{ij}^{k,\mathfrak{I}}+\left(\tilde{\sigma}_{j}^{k}\right)^{4}\left(u_{ij}^{k,\mathfrak{I}}\right)^{2}+\left(\tilde{\sigma}_{j}^{k}\right)^{2}\left(\tilde{\sigma}_{i}^{k}\right)^{2}\left[1-\left(\tilde{p}_{ij}^{k,\mathfrak{R}}\right)^{2}\right]\right\}^{3}}} \tag{7b}$$

According to Eq. (1) and Eq. (2b), D_B between TFs under the healthy state and the possibly damaged state are expressed as:

$$D_B^{\mathfrak{R}}\left(p\left(u_{ij}^{k,\mathfrak{R}}\right),p^{d}\left(u_{ij}^{k,\mathfrak{R}}\right)\right)=-\ln\left(\int\sqrt{p\left(u_{ij}^{k,\mathfrak{R}}\right)p^{d}\left(u_{ij}^{k,\mathfrak{R}}\right)}du_{ij}^{k,\mathfrak{R}}\right) \tag{8a}$$

$$D_B^{\mathfrak{I}}\left(p\left(u_{ij}^{k,\mathfrak{I}}\right),p^{d}\left(u_{ij}^{k,\mathfrak{I}}\right)\right)=-\ln\left(\int\sqrt{p\left(u_{ij}^{k,\mathfrak{I}}\right)p^{d}\left(u_{ij}^{k,\mathfrak{I}}\right)}du_{ij}^{k,\mathfrak{I}}\right) \tag{8b}$$

Fig. 2 presents two arbitrary PDFs of TFs and the area to be integrated in the computation of D_B between the PDFs. It can be found from Fig. 2 that the integrand of the Bhattacharyya coefficient is a unimodal function, which ensures the feasibility of Laplace's approximation to reduce computational cost of the integral since its premise is a single maximum over the domain. Therefore, it is reasonable to employ Bhattacharyya distance as the dissimilarity metric.

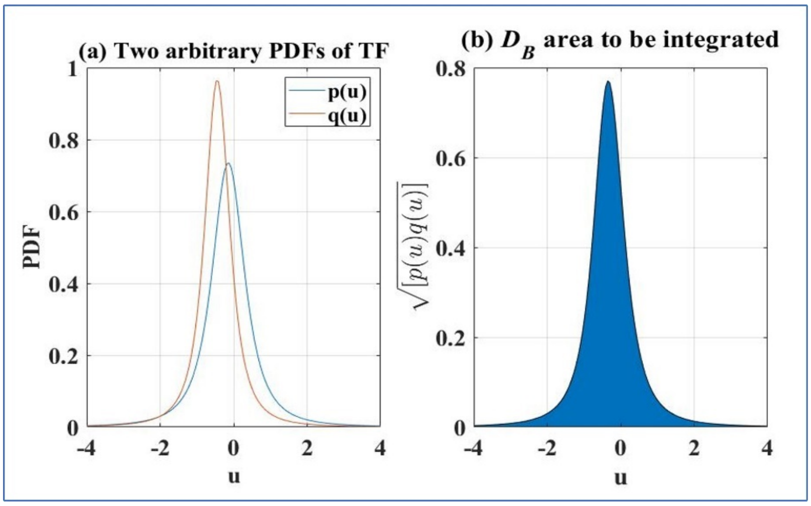

Figure 2. Schematic diagram of the Bhattacharyya distance $D_B\left(p(u),q(u)\right)$ between two arbitrary PDFs of TFs.

2.4 Laplace asymptotic expansion of Bhattacharyya distance of TFs

The application of Bhattacharyya distance in SHM is limited by its high computational cost and the stochastic feature of integrating the product of PDFs. To avoid the numerical integration involved in D_B, a Laplace method of asymptotic expansion is adopted here to avoid time-consuming numerical integration. Consider an integral with the following form:

$$I = \int_{\boldsymbol{\Omega}} p(\boldsymbol{\varphi}) q(\boldsymbol{\varphi}) \mathrm{d}\boldsymbol{\varphi} \tag{9}$$

where $p(\boldsymbol{\varphi})$ and $q(\boldsymbol{\varphi})$ are smooth functions for $\boldsymbol{\varphi}=\{\varphi_1, \varphi_2, \cdots, \varphi_q\}$ and $\boldsymbol{\Omega}$ is a subregion of $\Re^n$. Assume the integrand $p(\boldsymbol{\varphi})q(\boldsymbol{\varphi})$ has a single maximum $\boldsymbol{\varphi}^*$ inside the domain $\boldsymbol{\Omega}$, namely the global maximum over $\boldsymbol{\Omega}$. An asymptotic approximation for the integral $I(\boldsymbol{\varphi})$ is obtained by applying Laplace method of asymptotic expansion to it [36, 37]:

$$I(\boldsymbol{\varphi}) \approx (2\pi)^{\frac{q}{2}} p(\boldsymbol{\varphi}^*) q(\boldsymbol{\varphi}^*) \left| \boldsymbol{H}(\boldsymbol{\varphi}^*) \right|^{-\frac{1}{2}} \tag{10}$$

where q is the dimension of the vector $\boldsymbol{\varphi}$; $\left|\boldsymbol{H}(\boldsymbol{\varphi}^*)\right|$ refers to the determinant of the Hessian matrix of $f(\boldsymbol{\varphi}) = -\ln\left[p(\boldsymbol{\varphi})q(\boldsymbol{\varphi})\right]$ at $\boldsymbol{\varphi}=\boldsymbol{\varphi}^*$. The Hessian matrix is given by:

$$\boldsymbol{H}(\boldsymbol{\varphi}^*) = \begin{bmatrix} \dfrac{\partial^2 f}{\partial \varphi_1{}^2} & \dfrac{\partial^2 f}{\partial \varphi_1 \partial \varphi_2} & \cdots & \dfrac{\partial^2 f}{\partial \varphi_1 \partial \varphi_q} \\ \dfrac{\partial^2 f}{\partial \varphi_2 \partial \varphi_1} & \dfrac{\partial^2 f}{\partial \varphi_2{}^2} & \cdots & \dfrac{\partial^2 f}{\partial \varphi_2 \partial \varphi_q} \\ \vdots & \vdots & \ddots & \vdots \\ \dfrac{\partial^2 f}{\partial \varphi_q \partial \varphi_1} & \dfrac{\partial^2 f}{\partial \varphi_q \partial \varphi_2} & \cdots & \dfrac{\partial^2 f}{\partial \varphi_q{}^2} \end{bmatrix}_{\boldsymbol{\varphi}=\boldsymbol{\varphi}^*} \tag{11}$$

In the context of structural novelty detection, p_1 and p_2 corresponds to the square root of the real part of the PDFs of TFs under the healthy state and the possibly damaged state respectively, that is, $p_1\left(u_{ij}^{k,\Re}\right) = \sqrt{p\left(u_{ij}^{k,\Re}\right)}$ and $p_2\left(u_{ij}^{k,\Re}\right) = \sqrt{p^d\left(u_{ij}^{k,\Re}\right)}$. The real part of D_B between TFs under these two states is expressed using p_1 and p_2 according to Eq. (8a):

$$D_B^{\Re}\left(p\left(u_{ij}^{k,\Re}\right), p^d\left(u_{ij}^{k,\Re}\right)\right) = -\ln\left(\int p_1\left(u_{ij}^{k,\Re}\right) p_2\left(u_{ij}^{k,\Re}\right) du_{ij}^{k,\Re}\right) \tag{12}$$

Based on Eq. (10), the integration can be replaced by Laplace approximation:

$$D_B^{\Re}\left(p\left(u_{ij}^{k,\Re}\right), p^d\left(u_{ij}^{k,\Re}\right)\right) \approx -\ln\left((2\pi)^{\frac{1}{2}} p_1\left(u_{ij}^{k,\Re*}\right) p_2\left(u_{ij}^{k,\Re*}\right)\left|H\left(u_{ij}^{k,\Re*}\right)\right|^{-\frac{1}{2}}\right) \tag{13}$$

where $u_{ij}^{k,\Re*}$ denotes the global maximum of the integral $\int p_1 p_2 \mathrm{d}u_{ij}^{k,\Re}$, which is also the maximizing point of the integrand $p_1 p_2$ as well as $p\left(u_{ij}^{k,\Re}\right) p^d\left(u_{ij}^{k,\Re}\right)$. For the imaginary part $D_B^{\Im}$, its Laplace approximation can be derived similarly and is given by:

$$D_B^{\Im}\left(p\left(u_{ij}^{k,\Im}\right), p^d\left(u_{ij}^{k,\Im}\right)\right) \approx -\ln\left((2\pi)^{\frac{1}{2}} p_1\left(u_{ij}^{k,\Im*}\right) p_2\left(u_{ij}^{k,\Im*}\right)\left|H\left(u_{ij}^{k,\Im*}\right)\right|^{-\frac{1}{2}}\right) \tag{14}$$

The derivation of the global maximums $u_{ij}^{k,\Re*}$ and $u_{ij}^{k,\Im*}$, as well as the Hessian matrices $H\left(u_{ij}^{k,\Re*}\right)$ and $H\left(u_{ij}^{k,\Im*}\right)$, are presented in Appendix A and B. Based on the Laplace approximation method, D_B between two PDFs of TFs can be analytically derived without numerical integration, which significantly reduces the involved computational cost.

3. Novelty Detection Integrating Bhattacharyya Distance and Bayesian Resampling

3.1 Damage indicator based on Bhattacharyya distance

D_B between TFs under the healthy state and the possibly damaged state can be used for novelty detection. To improve the robustness of this method, data corresponding to different measurements and frequency points can be fused together. For a structure with n DOFs subject to arbitrary excitation under the healthy state, assume $\boldsymbol{y}(t) = \left\{y_1(t), y_2(t), \ldots, y_n(t)\right\}$ denotes the response vector of the structure. Then the TF of each DOF under the same reference response $y_j(t)$ can be expressed as a TF vector for both healthy and possibly damaged states:

$$\boldsymbol{T}_j^k = \left\{T_{1j}^{\ k}, T_{2j}^{\ k}, \ldots, T_{nj}^{\ k}\right\} \tag{15a}$$

$$\boldsymbol{T}_j^{d,k} = \left\{ T_{1j}{}^{d,k}, T_{2j}{}^{d,k}, \ldots, T_{nj}{}^{d,k} \right\} \tag{15b}$$

One can calculate the values of D_B between each pair of TFs in the vector under the healthy state and the possibly damaged state, and the mean of these D_B values represent the D_B at the frequency ω_k. Furthermore, it is common to select TFs within a frequency band $[\omega_1, \omega_2]$ instead of at a single frequency point to formulate the damage indicator [7]. The damage indicator is obtained by averaging the values of D_B over the frequency band:

$$DI_B{}^{\Re} = \frac{1}{n_\omega (n-1)} \sum_{k=k_1}^{k_2} \sum_{j=1, j \neq i}^{n} D_{B_{ij}}{}^{k,\Re} \left(p\left(u_{ij}{}^{k,\Re}\right), p^d\left(u_{ij}{}^{k,\Re}\right) \right) \tag{16a}$$

$$DI_B{}^{\Im} = \frac{1}{n_\omega (n-1)} \sum_{k=k_1}^{k_2} \sum_{j=1, j \neq i}^{n} D_{B_{ij}}{}^{k,\Im} \left(p\left(u_{ij}{}^{k,\Im}\right), p^d\left(u_{ij}{}^{k,\Im}\right) \right) \tag{16b}$$

where n_ω refers to the total number of frequency points within the frequency band $[\omega_1, \omega_2]$, and $n_\omega = k_2 - k_1$; $D_{B_{ij}}{}^{k,\Re}$ and $D_{B_{ij}}{}^{k,\Im}$ denote the real and imaginary parts of D_B between T_{ij}^k and $T_{ij}^{d,k}$. The damage indicator will be further employed for novelty detection in the next section in tandem with the state discrimination methods.

3.2 Bayesian resampling-assisted novelty detection

State discrimination is a crucial step in structural novelty detection to determine whether each sample comes from the healthy state or the damaged state when given a set of damage indicator samples. In this study, two commonly used methods including the GMM clustering method as well as the threshold method will be utilized for state discrimination. It is worth noting that, the DI_B-based state discrimination would be affected by the variability of the model parameters $\boldsymbol{\Theta}_k$ involved in the complex-Gaussian ratio distribution, which represents the unresolved uncertainty given measured data and model assumptions. To accommodate the variability of the statistical model parameters $\mathbf{\Theta}_k$, a Bayesian resampling scheme is proposed to achieve the posterior distribution of the model parameters $\mathbf{\Theta}_k$. Monte Carlo simulation can be performed to generate samples from the Gaussian distribution of $\mathbf{\Theta}_k$, which will be used to calculate the corresponding samples of damage indicator shown in Eq. (16). As a result, these DI_B samples will be used to conduct GMM clustering and compared with the threshold value for state discrimination.

3.2.1 Bayesian resampling scheme

The Bayesian resampling scheme is composed of two steps. First, Bayesian inference is performed for the parameters of the probabilistic model of TF, $\mathbf{\Theta}_k$, to accommodate their variability due to measurement noise and modelling error. It can be proved that $\mathbf{\Theta}_k$ can be approximated by a Gaussian PDF. Second, Monte Carlo simulation is performed to generate samplings from the Gaussian distribution of $\mathbf{\Theta}_k$.

Conditioned on N sets of TF measurements within the frequency band $\mathbf{\Psi} = \left[k_1\Delta\omega, k_2\Delta\omega,\right]$, which is denoted by $\mathbf{\Phi} = \left\{\left(u_{ij}^{k}\right)_n, n = 1, 2, \ldots, N; k = k_1, k_1+1, \ldots, k_2\right\}$, the statistical parameters formulating the PDFs of each TF shown in Eq. (5) are denoted by $\mathbf{\Theta}_k = \left\{\sigma_i^k, \sigma_j^k, \rho_{ij}^{k,\Re}, \rho_{ij}^{k,\Im}\right\}, k \in \left[k_1, k_2\right]$. According to Bayes' theorem, the posterior probability of the statistical parameters $\mathbf{\Theta}_k$ given $\mathbf{\Phi}$ can be calculated as:

$$p\left(\mathbf{\Theta}_k \middle| \mathbf{\Phi}\right) = c_o\, p\left(\mathbf{\Theta}_k\right) p\left(\mathbf{\Phi} \middle| \mathbf{\Theta}_k\right) \tag{17}$$

where c_o is a normalized constant; $p\left(\mathbf{\Theta}_k\right)$ refers to the prior probability of $\mathbf{\Theta}_k$; and $p\left(\mathbf{\Phi} \middle| \mathbf{\Theta}_k\right)$ is the likelihood function given by:

$$p\left(\mathbf{\Phi} \middle| \mathbf{\Theta}_k\right) = \prod_{n=1}^{N} p\left(\left(u_{ij}{}^{k,\Re}\right)_n \middle| \mathbf{\Theta}_k\right) p\left(\left(u_{ij}{}^{k,\Im}\right)_n \middle| \mathbf{\Theta}_k\right) \tag{18}$$

The posterior distribution of $\mathbf{\Theta}_k$ is proportional to the likelihood function when a non-informative prior is used [33]:

$$p\left(\mathbf{\Theta}_k \middle| \mathbf{\Phi}\right) \propto \exp\left(-\chi\left(\mathbf{\Theta}_k\right)\right) \tag{19}$$

where $\chi\left(\mathbf{\Theta}_k\right)$ denotes the negative log-likelihood function (NLLF) and is given by:

$$\chi\left(\mathbf{\Theta}_k\right) = \chi^{\Re}\left(\mathbf{\Theta}_k\right) + \chi^{\Im}\left(\mathbf{\Theta}_k\right) = \sum_{n=1}^{N} \ln\left[p\left(\left(u_{ij}^{k,\Re}\right)_n \middle| \mathbf{\Theta}_k\right)\right] + \sum_{n=1}^{N} \ln\left[p\left(\left(u_{ij}^{k,\Im}\right)_n \middle| \mathbf{\Theta}_k\right)\right] \tag{20}$$

Assume $\widehat{\mathbf{\Theta}}_k = \left\{\widehat{\sigma}_i^k, \widehat{\sigma}_j^k, \widehat{\rho}_{ij}^{k,\Re}, \widehat{\rho}_{ij}^{k,\Im}\right\}$ denotes the most probable values of the statistical parameters and $H\left(\widehat{\mathbf{\Theta}}_k\right)$ denotes the Hessian matrix of $\chi\left(\mathbf{\Theta}_k\right)$ at the most probable value $\widehat{\mathbf{\Theta}}_k$. The posterior probability $p\left(\mathbf{\Theta}_k \middle| \mathbf{\Phi}\right)$ can be well approximated by a multivariate Gaussian distribution [38] with mean $\widehat{\mathbf{\Theta}}_k$ and covariance matrix $H^{-1}\left(\widehat{\mathbf{\Theta}}_k\right)$, based upon which the statistical parameters can be acquired by random sample generation, and the variability of statistical parameters of the probabilistic model of TF can be accommodated. In the procedure of novelty detection, the Bayesian resampling scheme would be used to generate samples of $\mathbf{\Theta}_k$ and compute DI_B samples to improve the robustness of the proposed method against uncertainties.

3.2.2 Novelty detection based on GMM clustering

GMM clustering is one of the most commonly employed clustering approaches in damage detection [21, 39, 40]. Their work shows that the GMM-based method outperforms some classic damage detection methods on the standard dataset [21, 39, 40]. In this work, the DI_B samples are divided into two clusters via GMM clustering with one representing the healthy state and the other denoting the damaged state. It has been reported that the performance of GMM could be affected by the initial guess of centroids of the two clusters [41]. To overcome the limitation of conventional method by assigning the values randomly, the initial centroids of the two clusters in GMM clustering in this study are determined via a Monte Carlo discordancy testing by accommodating the uncertainties involved in the statistical parameters of PDF of TFs (i.e., $\mathbf{\Theta}_k$). The main procedures of novelty detection based on Bayesian resampling scheme-assisted GMM clustering are outlined as follows:

(i) Based on the Bayesian resampling scheme, one can obtain the posterior distribution of the model parameters $\mathbf{\Theta}_k$ using the measurements under the normal condition according to Section 3.2.1;

(ii) Generate the samples according to the Gaussian distribution of $\mathbf{\Theta}_k$ over the selected frequency band;

(iii) DI_B values are calculated for all the samples of $\mathbf{\Theta}_k$ in the baseline condition using Eq. (16), while the largest and smallest values are stored;

(iv) The steps of (i)-(iii) are repeated for a large number of trials to formulate an array containing the largest and smallest DI_B values corresponding to all of the trails;

(v) Based on the samples of the baseline condition generated in step (iv), the initial centroids of two clusters can be determined based on the criteria that the range of the first cluster should cover most of the samples from the baseline condition while the samples exceeding the range could be predicted to belong the other cluster. The initial centroid of the first cluster and the second cluster are denoted by $DI_{baseline}$ and $\alpha DI_{baseline}$, respectively. $DI_{baseline}$ is set by using the mean of the samples generated in step (iv), while the radius r of the clusters can be obtained correspondingly based on 1% tests of discordancy, which indicates that the first cluster should cover 99% DI_B samples from the baseline condition.

As a result, the initial centroid of the second cluster could be set to be the sum of $DI_{baseline}$ and two times of the radius (i.e., $2r$), and α can be determined by taking the ratio of $\left(DI_{baseline}+2r\right)$ to $DI_{baseline}$;

(vi) Repeat the steps of (i)-(ii) for different damage states based on their corresponding measurements to formulate a number of DI_B values under different states;

(vii) Initialize GMM clustering based on the initial centroids obtained in step (v), following which the expectation maximization (EM) algorithm is conducted for DI_B values under different states (see step (vi)) to evaluate the posterior probabilities of each sample belonging to each cluster iteratively until the convergence criterion is achieved. One can refer to [42] for more details on GMM clustering;

(viii) Based on the clustering result, the DI_B samples assigned to the first cluster are predicted to belong to a normal condition, while the samples assigned to the other cluster are labelled as a potential damaged state.

3.2.3 Novelty detection based on threshold value

A Monte Carlo discordancy testing motivated by Ref. [19] was utilized to arrive at the threshold value by properly accommodating the uncertainties involved in the statistical parameters $\boldsymbol{\Theta}_k$. The major procedures are shown as follows:

(i) Infer the posterior distribution of the model parameters $\boldsymbol{\Theta}_k$ based on the Bayesian resampling scheme according to Section 3.2.1;

(ii) Based on the Gaussian distribution of $\boldsymbol{\Theta}_k$, one can generate random samples over a specific frequency band according to the Bayesian resampling scheme;

(iii) DI_B values are calculated for all the samples of $\boldsymbol{\Theta}_k$ using Eq. (16), while the largest values are picked out;

(iv) The steps of (i)-(iii) are repeated for a large number of times and the largest DI_B are ordered in terms of magnitude;

(v) The critical value for 1% tests of discordancy is chosen as the threshold value so that a state with damage indices larger than the threshold value is suggested to be labelled as potential damage.

4. Procedures of Structural Novelty Detection

The novelty detection approach illustrated in Section 2 and Section 3 is summarized in Fig. 3, which mainly involves the three following steps:

Step (1): Bayesian resampling to generate samples of $\mathbf{\Theta}_k$ under different states

- Acquire n_o response measurements of a structure under each structural state;
- Infer the posterior distribution of the model parameters $\mathbf{\Theta}_k$ in a Bayesian framework;
- Perform Monte Carlo simulation to generate samples from the Gaussian distribution of $\mathbf{\Theta}_k$.

Step (2): Calculating DI_B for different samples of $\mathbf{\Theta}_k$ under different states

- Calculate the Bhattacharyya distance of transmissibility using Laplace asymptotic expansion within a frequency band $[\omega_1, \omega_2]$ according to Eq. (13) and (14);
- Compute the damage indicator DI_B corresponding to different states based on Eq. (16);
- Repeat the above steps for different samples of $\mathbf{\Theta}_k$ to obtain a number of DI_B samples.

Step (3): Novelty detection based on GMM clustering and threshold value

- **For the GMM-based novelty detection method:** Set $DI_{baseline}$ as the initial centroid of the first cluster, and set $\alpha DI_{baseline}$ as the initial centroid of the second cluster with $DI_{baseline}$ and α being determined by the Monte Carlo discordancy testing according to Section 3.2.2;

Then divide the DI_B samples into 2 clusters based on GMM clustering; The DI_B samples assigned to cluster 1 are predicted to be from the normal condition, while the samples assigned to cluster 2 are predicted to be from a damaged state.

- **For the threshold-based novelty detection method:** Construct a 1% exclusive threshold value using the Monte Carlo discordancy testing according to Section 3.2.3; Determine the damage state through checking if the damage index exceeds the threshold value or not.

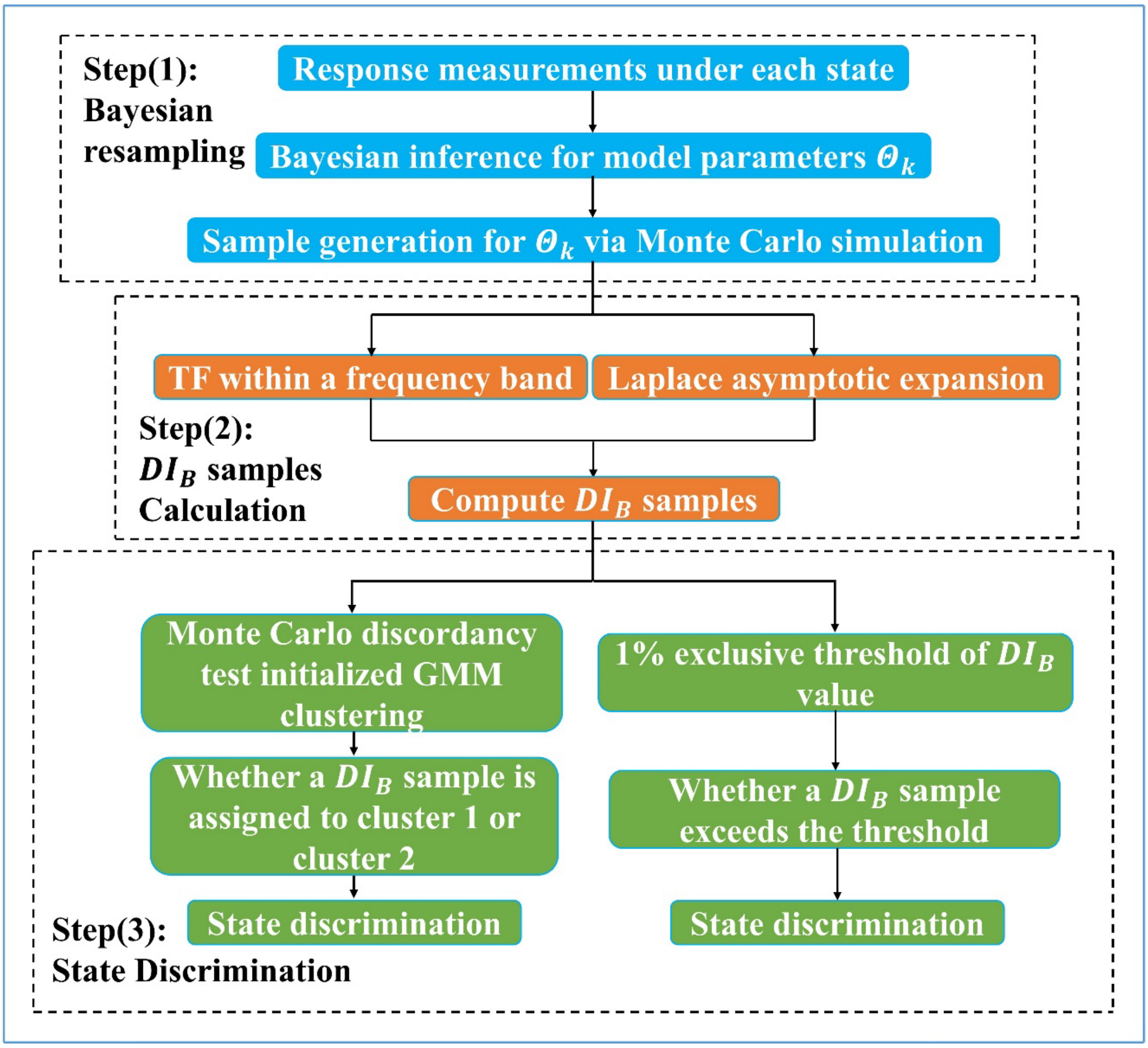

Figure 3. Flowchart of the structural novelty detection algorithms proposed in this study.

5. Case Studies

The efficiency and accuracy of the proposed novelty detection method is investigated via two realistic case studies: a vibration test of a three-story laboratory building structure and a progressive damage test of the S101 bridge. Different scenarios concerning structural damage as well as environmental and operational variabilities (EOVs) are simulated in these case studies, so they can be regarded as representative operational conditions in real applications. The measured data are used to infer the posterior distribution of the probabilistic model of TFs, from which the statistical parameter samples are generated by the Bayesian resampling method described in Section 3.2.1. Consequently, the DI_B values can be calculated based on the D_B of TFs using Laplace asymptotic expansion. Then the GMM method and the threshold method are conducted for novelty detection on these DI_B samples.

5.1 Case Study 1: A three-story building structure

A benchmark dataset from a three-story laboratory building structure produced by Los Alamos National Laboratory [43] is adopted to explore the performance of the proposed method for novelty detection with the presence of EOVs. The three-story building structure is shown in Fig. 4, which is Fig. 1 in [43]. In the experimental study conducted to obtain the benchmark dataset, the base of the building structure was mounted on rails that allowed movement in the X-direction only. The structure was excited at the base via an electrodynamic shaker. Four accelerometers were mounted at the center line of the base and each floor to measure the responses, and a load cell was used to collect the signal of input. The sensors' location as well as linear bearings were designed to minimize the torsional effect. Seventeen different states were tested in the study, the details of which are shown in Table 1.

Figure 4. The three-story building structure and shaker in the experimental study (from [43]).

Table 1. Different states tested in the experimental study (reproduced from [43])

Label	**State Condition**	**Description**
State 1	Undamaged	Baseline condition
State 2	Undamaged	Added mass (1.2 kg) at the base
State 3	Undamaged	Added mass (1.2 kg) on the first floor
State 4	Undamaged	87.5% stiffness reduction in column 1BD
State 5	Undamaged	87.5% stiffness reduction in column 1AD and 1BD
State 6	Undamaged	87.5% stiffness reduction in column 2BD
State 7	Undamaged	87.5% stiffness reduction in column 2AD and 2BD
State 8	Undamaged	87.5% stiffness reduction in column 3BD
State 9	Undamaged	87.5% stiffness reduction in column 3AD and 3BD
State 10	Damaged	Gap = 0.20 mm
State 11	Damaged	Gap = 0.15 mm
State 12	Damaged	Gap = 0.13 mm
State 13	Damaged	Gap = 0.10 mm
State 14	Damaged	Gap = 0.05 mm
State 15	Damaged	Gap (0.20 mm) and mass (1.2 kg) at the base
State 16	Damaged	Gap (0.20 mm) and mass (1.2 kg) on the first floor
State 17	Damaged	Gap (0.10 mm) and mass (1.2 kg) on the first floor

As can be seen from the table, apart from the baseline condition, sixteen other states were also simulated, with eight states (states 2-9) representing EOVs and eight states (states 10-17) representing structural damage. The EOVs were simulated by changing the stiffness and mass of certain stories. Structural damage was introduced by a bumper mechanism that simulated the nonlinearity of repeated impact, and different damage extents were represented by changing the gap between the bumper and the column. The load cell and accelerometers constituted a data acquisition system with five channels. Fifty measurements were conducted in each state, with a sampling frequency of 320Hz and a duration of 25.6s. Therefore, 8192 discretized data points were acquired in each channel for one measurement, and an overall dataset with dimensions of $8192 \times 5 \times 850$ was obtained.

The variation of $D_B^{T_{4,2}^{\mathfrak{R}}}$ (the D_B between $T_{4,2}^{\mathfrak{R}}$ under different states) at each frequency point within the frequency band [0.4Hz, 100Hz] is displayed in Fig. 5(a), and the variation of PSD with frequency for state 1 is presented in Fig. 5(b). From these figures, one can conclude that the peaks of $D_B^{T_{4,2}^{\mathfrak{R}}}$ values correspond to the peaks of the PSD, indicating that the most significant variation of $D_B^{T_{4,2}^{\mathfrak{R}}}$ occurs around the resonant frequencies of the structure.

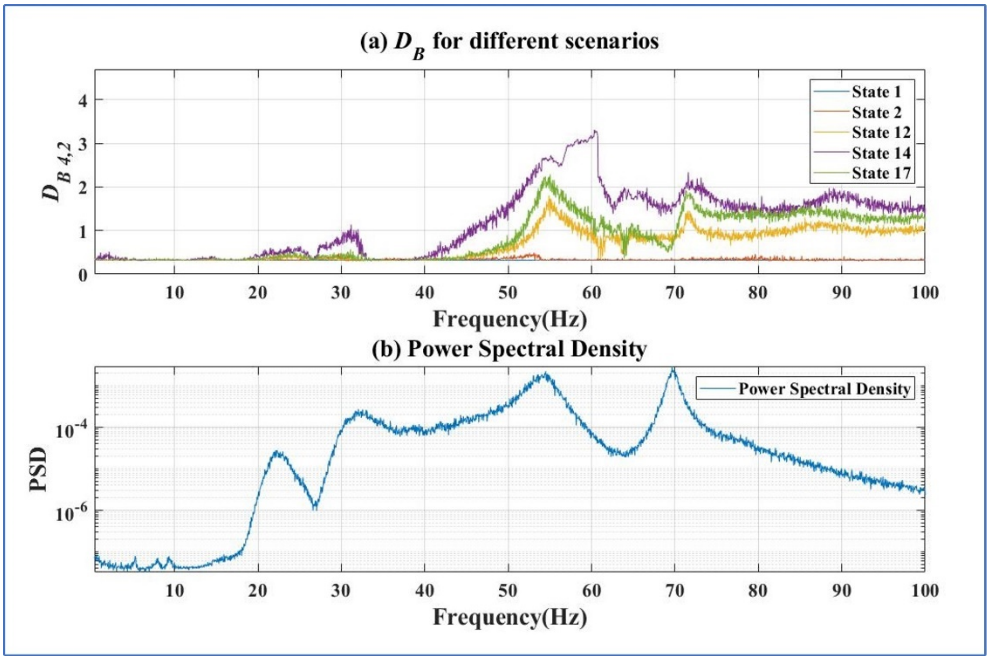

Figure 5. (a) The variation of $D_B^{T_{4,2}^{\mathfrak{R}}}$ under states 1, 2, 12, 14, and 17 at different frequency points; (b) The variation of power spectral density with respect to frequency for state 1.

In SHM, one hopes to build a novelty detection system sensitive to damage but insensitive to EOVs, which is usually achieved via a data normalization [44-46] or feature selection step [47-49]. In this work, the feature selection method introduced in Ref. [50] is followed to remove the sensitivity to EOVs and 50 frequency points are selected. The advantage of this method is that it requires neither damage state data nor a complex training phase [39]. Fig. 6 presents the DI_B values under the 17 states after feature selection. It is clearly found the increase of the DI_B value when damage (nonlinearities) is introduced, demonstrating the capability of the proposed damage indicator to measure the effect of nonlinearity in combination with the feature selection method. In addition, it can be found that the DI_B values increase with the damage level, illustrating its capability of indicating the relative damage extent.

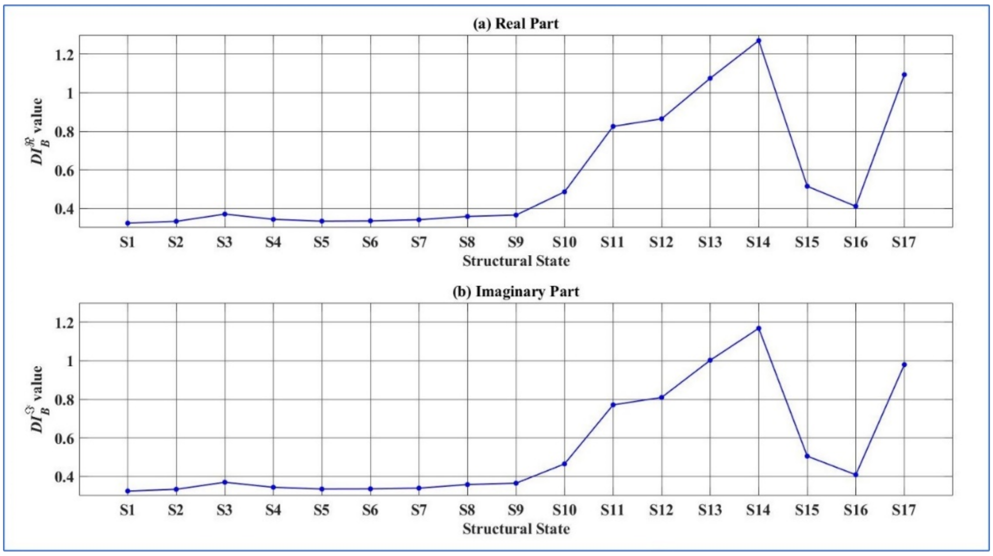

Figure 6. (a) Real part of DI_B values and (b) Imaginary part of DI_B values under different states.

To accommodate the uncertainties of the statistical parameters of the probabilistic model of TF, 120 DI_B samples are computed under each state based on the Bayesian resampling scheme. The total 2040 DI_B samples are divided into two clusters via GMM clustering. According to the Monte Carlo method described in Section 3.2.2, $DI_{baseline}$ and α are set as 0.4124 and 2.04 for the $DI_B^{\Re}$ based GMM clustering, while for the $DI_B^{\Im}$ based GMM clustering, $DI_{baseline}$ and α are chosen as 0.4101 and 2.02, respectively. Fig. 7 presents the clustering results of the real and imaginary parts of DI_B samples, from which one can conclude that most data points are correctly classified via the DI_B-GMM method as cluster 1 denotes the normal condition and cluster 2 represents the damaged state. Then a 1% exclusive threshold of DI_B is established based on the Monte Carlo method described in 3.2.3, and the novelty detection results of this method is shown in Fig. 8. It can be found that the threshold-based method results in more false negative indications than the GMM-based method, and all false negatives occur at the lowest damage states (0.20 mm Gap).

To present the novelty detection result more intuitively, the false positive and false negative rates are adopted here to quantitatively depict the performance of the proposed method:

$$FPR = \frac{FP}{TN + FP} \times 100\% \tag{21a}$$

$$FNR = \frac{FN}{FN + TP} \times 100\% \tag{21b}$$

where FPR and FNR denote the false positive and false negative rates; TP, TN, FP, and FN are the number of true positives, true negatives, false positives, and false negatives, respectively. Fig. 9 presents the confusion matrices of the GMM-based method and the threshold-based method. It can be found that for the $DI_B^{\Re}$-GMM method, there are 9 false positive indications and 31 false negative indications across the dataset of 2040 observations. These results correspond to a FPR of 0.83% and a FNR of 3.23%, giving a total accuracy of 98.04%. For the $DI_B^{\Re}$-threshold method, there are no false positives but 286 false negatives across the dataset. The FPR and FNR are 0% and 29.79% respectively, giving an accuracy of 85.98%. Therefore, the accuracy of the $DI_B^{\Re}$-GMM method is 12.06% higher than that of the $DI_B^{\Re}$-threshold method. Meanwhile, for the $DI_B^{\Im}$-based novelty detection, the GMM-based method has an accuracy 13.58% higher than the threshold-based method.

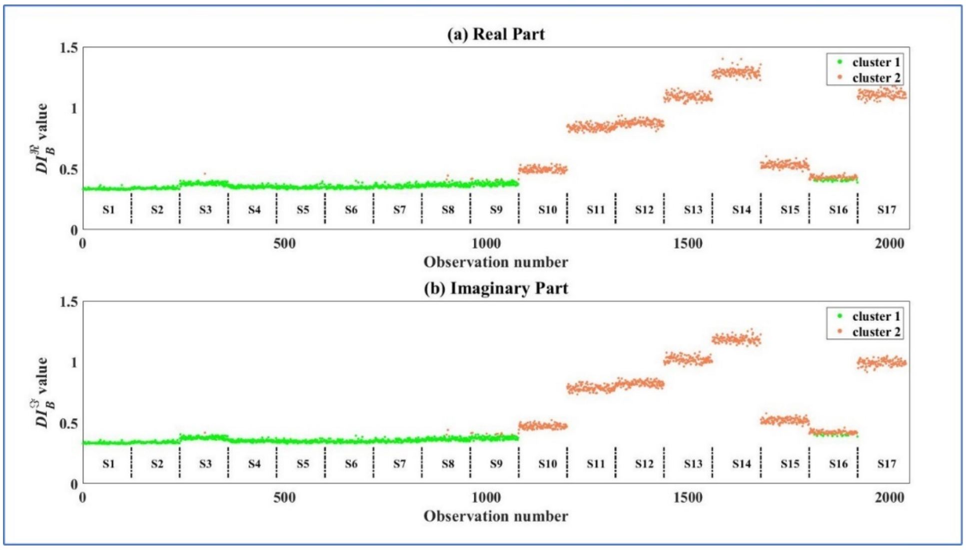

Figure 7. Novelty detection result of: (a) $DI_B^{\Re}$-GMM method; (b) $DI_B^{\Im}$-GMM method in the experimental study.

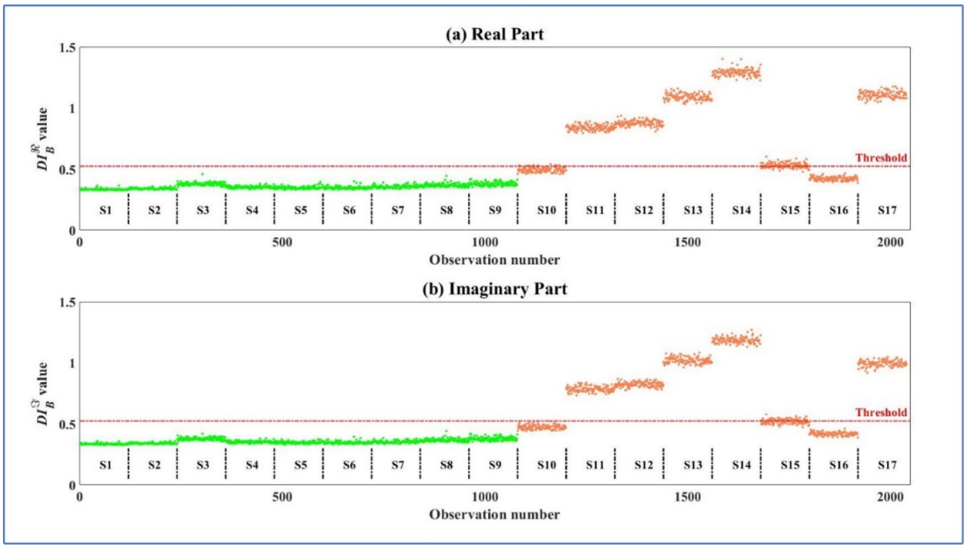

Figure 8. (a) $DI_B^{\Re}$ values and (b) $DI_B^{\Im}$ values for healthy (green) and damaged (orange) states with respect to the 1% threshold value (dashed line) established via the Monte Carlo method.

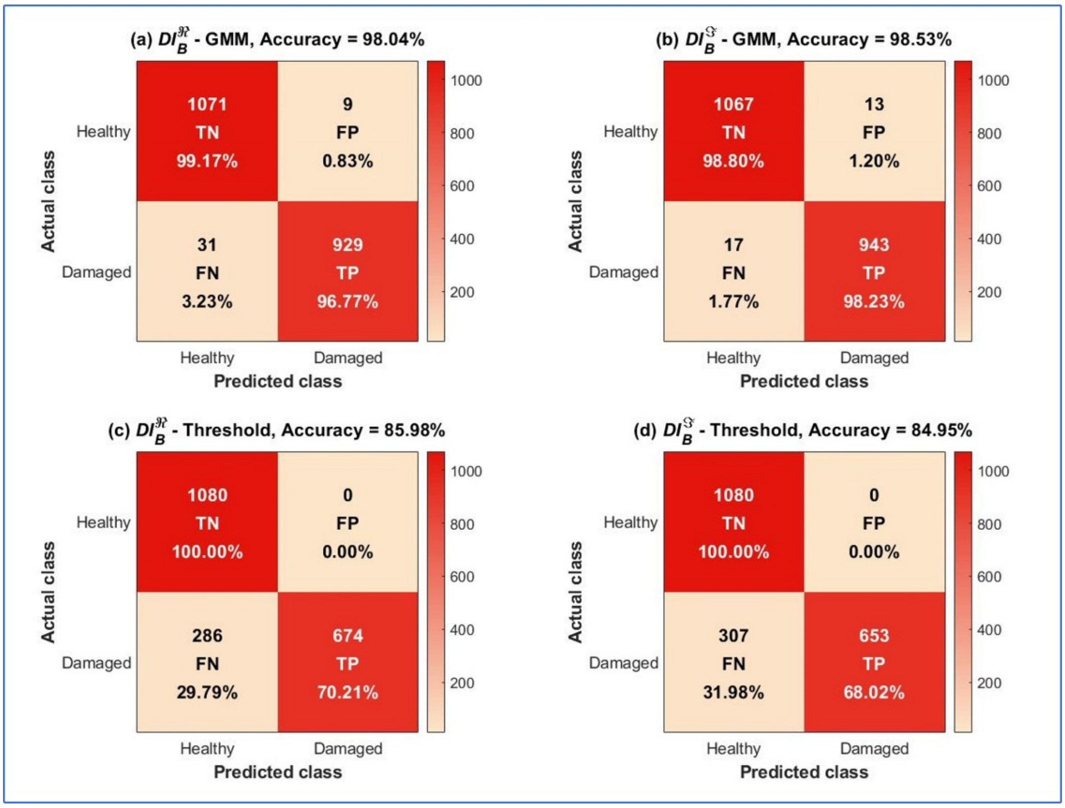

Figure 9. The confusion matrices of the novelty detection result of: (a) $DI_B^{\Re}$-GMM method; (b) $DI_B^{\Im}$-GMM method; (c) $DI_B^{\Re}$-threshold method; (d) $DI_B^{\Im}$-threshold method.

In order to further assess the proposed novelty detection methods, a Mahalanobis squared distance (MSD) based novelty detection method is adopted on this dataset for comparison. The MSD of the real and imaginary parts of TFs is employed as the damage indicator, respectively. MSD is a normalized measure of the distance between an observation and the mean of the sample distribution and is defined as:

$$MSD_{\zeta} = \left(\boldsymbol{x}_{\zeta} - \overline{\boldsymbol{\mu}}\right)^{T} \boldsymbol{\Sigma}^{-1} \left(\boldsymbol{x}_{\zeta} - \overline{\boldsymbol{\mu}}\right) \tag{22}$$

where $\boldsymbol{x}_{\zeta}$ is the potential outlier datum, $\overline{\boldsymbol{\mu}}$ is the mean vector of the sample observations and $\boldsymbol{\Sigma}$ is the sample covariance matrix. $\overline{\boldsymbol{\mu}}$ and $\boldsymbol{\Sigma}$ are derived using the samples from the normal condition (states 1-9), and a 1% exclusive threshold is constructed following the Monte Carlo method described in [19] for novelty detection. It is worth noting that the dimension of observations is determined as 50 according to the number of frequency points within the selected frequency band. Fig. 10 presents the novelty detection results of the MSD-based method, while Fig. 11 shows the corresponding confusion matrices. It can be found that the MSD-based method suffers from false negative indications with an accuracy lower than the DI_B-based methods. The reason could be that the implicit Gaussian assumption involved in MSD is not able to accommodate the statistical properties of scalar TFs appropriately, which demonstrates the advantage of adopting the probabilistic model of circularly-symmetric complex normal ratio distribution.

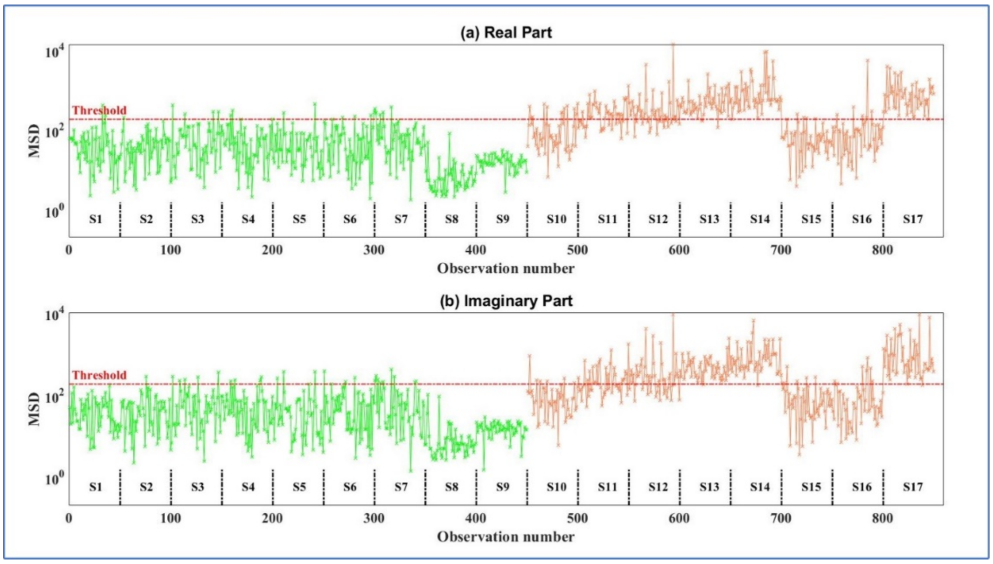

Figure 10. Mahalanobis squared distances of (a) real part of TFs; (b) imaginary part of TFs for healthy (green) and damaged (orange) states with respect to the 1% threshold value (dashed line) established via Monte Carlo simulation.

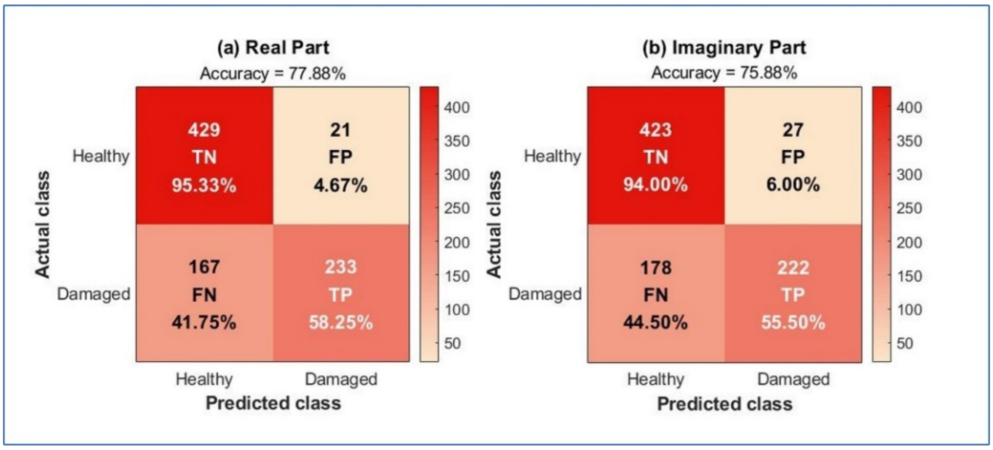

Figure 11. The confusion matrices of the novelty detection result of (a) MSD-$TF^{\Re}$ method; (b) MSD-$TF^{\Im}$ method.

Then the sensitivity of the DI_B-GMM method to the choice of α is investigated. The FPR, FNR, and accuracy of novelty detection results with respect to different levels of α are shown in Table 2. The results show that the Monte Carlo simulation-based initialization approach leads to a more reasonable α value with good performance for the DI_B-GMM method, while the conventional random initialization approach (randomly select two DI_B samples as initial centroids) is more likely to suffer from choosing unreasonable α values with worse novelty detection results.

Table 2. Novelty detection results with respect to different levels of α

	$DI_B^{\Re}$-GMM			$DI_B^{\Im}$-GMM		
α	FPR	FNR	Accuracy	FPR	FNR	Accuracy
1.1	0.83%	3.23%	98.04%	1.20%	1.77%	98.53%
1.2	0.83%	3.23%	98.04%	1.20%	1.77%	98.53%
1.3	0.83%	3.23%	98.04%	1.20%	1.77%	98.53%
1.5	0.83%	3.23%	98.04%	1.20%	1.77%	98.53%
2.0	0.83%	3.23%	98.04%	1.20%	1.77%	98.53%
2.5	0%	37.08%	82.55%	1.20%	1.77%	98.53%
3.0	0%	37.19%	82.50%	1.20%	1.77%	98.53%
4.0	0%	37.19%	82.50%	1.20%	1.77%	98.53%
5.0	0%	37.19%	82.50%	0%	95.52%	55.05%

5.2 Case Study 2: Field test of the S101 bridge

To investigate the performance of the novelty detection method for real structures, response measurements from a progressive damage test conducted on the S101 bridge are adopted for structural novelty detection. The S101 bridge was a post-tensional three-span prestressed concrete bridge located in Austria. The main span of the bridge was 32m long, whereas the two side spans were 12m long. The cross-section of the bridge was 7.2m wide and was in the form of a double-webbed T-beam with a width of 0.6m for each web. The height of the beam varied from 0.9m at the mid-span to 1.7m over the piers.

Aiming to analyze the effects of slowly progressing damage on structural dynamic response, the demolition of the bridge was accompanied by a progressive damage test [51, 52]. The test was composed of two major parts: in the former part, the northwestern pier of the bridge was lowered by about 3cm stepwise, whereas in the latter part several tendons were cut to simulate the effects of local prestressing reinforcement loss. The damage actions during the test as well as their effects are shown in Table 3. For more details about the S101 bridge and the progressive damage test, refer to [51].

Table 3. Notation of consecutive damage actions acted on the S101 bridge and their effects (reproduced from Table 1 in [52]).

State No.	Damage action	Damage effect
A	No action	♦ Baseline
B	Begin of cutting through the north-western pier	♦ Neither extra cracking nor increase of existing cracks are observed
C	End of second cut through the pier	♦ Formation of an extra hinge just above the foundation, which itself is equivalent to a constructive fixed support
D	1st step of the pier settlement (10mm)	♦ Moderate noise
E	2nd step of the pier settlement (20	♦ Horizontal cracks are found

	mm)	in neighboring pier
F	3rd step of the pier settlement (27 mm)	♦ Settling of bridge deck until reaching the elastic limits, support is not lost completely due to the hydraulic jack
G	Inserting steel plates	♦
H	Uplifting the damaged pier	♦ Some occurred cracks are closed ♦ The hinge caused by cutting remains
I	Exposing cables and cutting of 1st cable	♦ Reduction of prestressing without indication of the change of conditions
J	Cutting through 2nd cable	♦ No obvious influence on structural behavior since bridge is not loaded by traffic
K	Cutting through 3rd cable	♦
L	Partly cutting of 4th cable	♦ The extra prestressing reservoir is run out

In the progressive damage test, the dynamic responses of the bridge were measured using 15 sensors located on the bridge deck. The sampling frequency of these sensors was set as 500Hz. Each sensor had three channels to measure the vertical, longitudinal, and transversal responses. The duration of each measurement was set as 5.5min, and a series of datasets containing 45 channels with 165000 data points in each channel were produced. It is worth noting that misty winter weather just below freezing was dominant during the measurement period [52], so environmental variability was negligible in this test.

In the present study, the measured vertical responses from the progressive damage test are used to construct TFs. For the undamaged state A, the obtained dataset is divided into two groups, namely A0 and A1. The DI_B between TFs under A0 and A1 is the DI_B value under state A. The frequency band for calculating DI_B values is selected as [0.03Hz, 50Hz]. The variation of DI_B value with respect to different damage actions is shown in Fig. 12. Consistent with the first case study, it can also be found from Fig. 12 that the DI_B values increase with the damage extent. For states B and C, the damage extent increases with the cutting process, but the support is not completely lost. Therefore, the DI_B value increases accordingly but is not much larger than the baseline. For states D to F, serious damage occurs with the settlement of the column, corresponding to rapid increase in DI_B value. For states G and H, repair work is conducted, and the DI_B value decreases to a lower level. States I to L correspond to the damage scenario induced by tendon cutting. For states I and L, DI_B values are much larger than baseline because of the reduction of prestressing, whereas for states J and K, DI_B values are only slightly higher than the baseline since the bridge is not loaded by traffic.

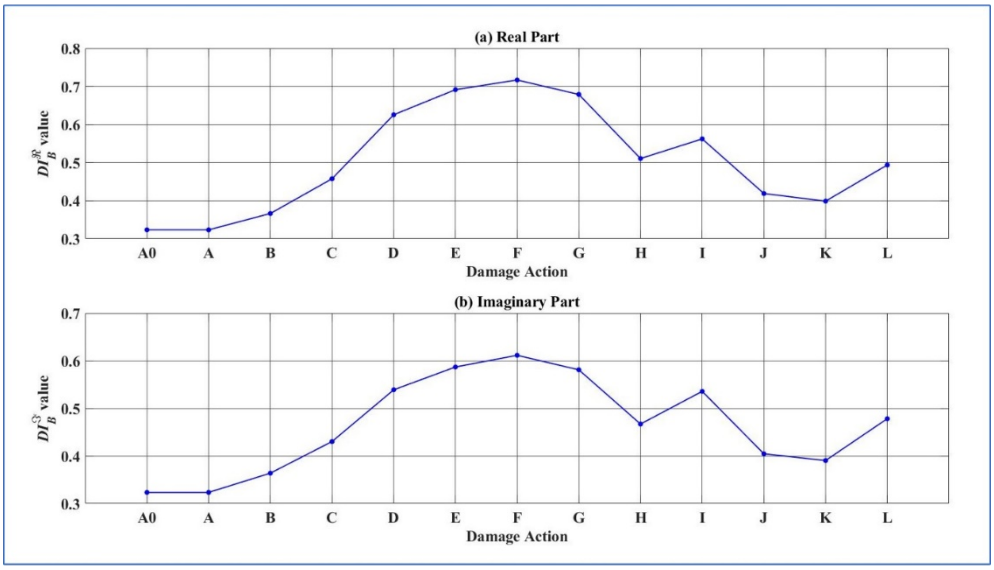

Figure 12. (a) Real part of DI_B values and (b) Imaginary part of DI_B values under different damage actions in the progressive damage test.

Then 100 DI_B samples under each state are computed based on Bayesian resampling to accommodate the uncertainties of the statistical parameters. The 1300 DI_B samples are divided into two clusters using GMM clustering initialized via the Monte Carlo method. Fig. 13 presents the novelty detection results of the DI_B-GMM method. Then a 1% exclusive threshold is established for novelty detection and the results are shown in Fig. 14. The confusion matrices of these novelty detection results are presented in Fig. 15. From these figures, one can conclude that both the GMM-based method and the threshold-based method exhibit good performance in the S101 dataset with the accuracy exceeding 99.5%. All damage actions introduced in the progressive damage test are detected, which demonstrates the potential of the proposed novelty detection methods for implementing on real structures.

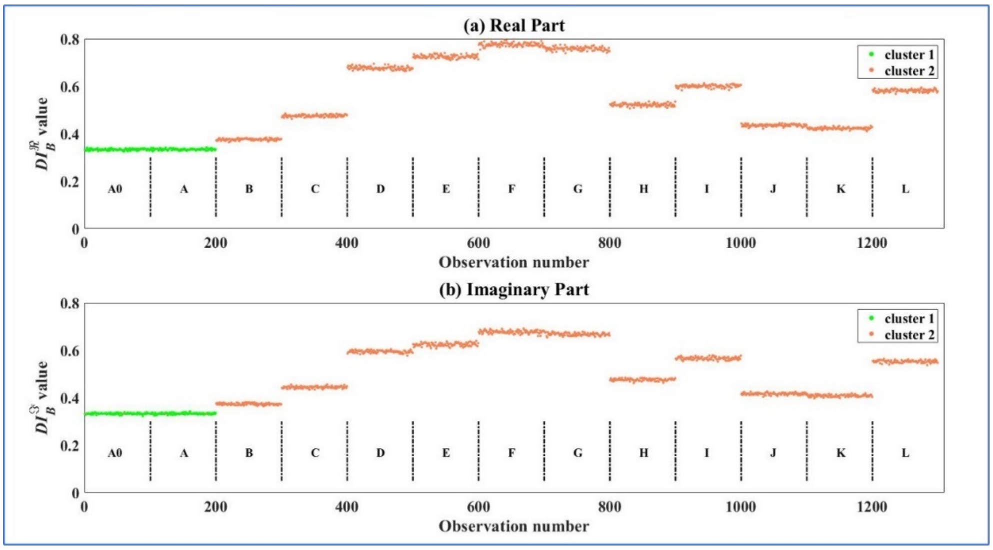

Figure 13. Novelty detection result of: (a) $DI_B^{\Re}$-GMM method; (b) $DI_B^{\Im}$-GMM method in the S101 case study.

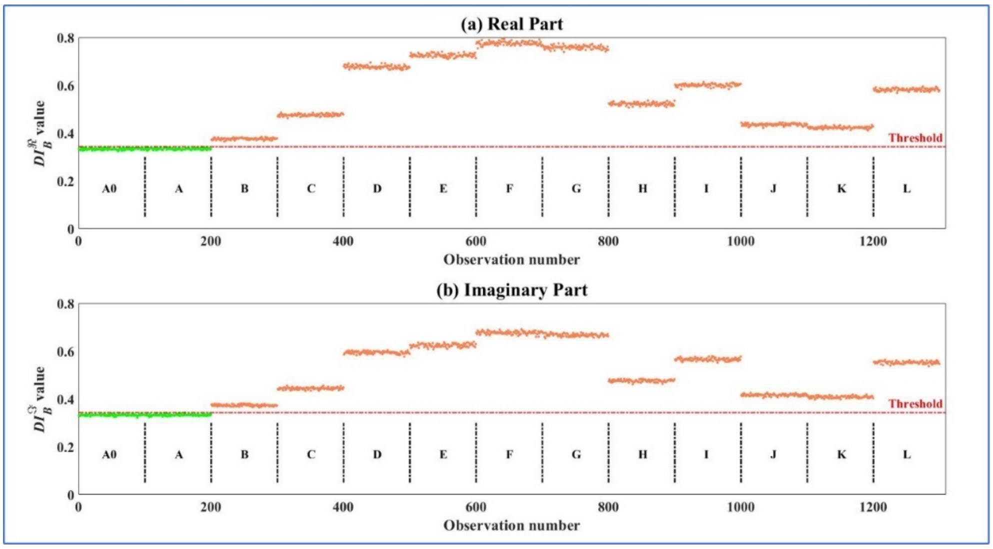

Figure 14. (a) $DI_B^{\Re}$ values and (b) $DI_B^{\Im}$ values for healthy (green) and damaged (orange) states with respect to the 1% threshold value (dashed line) established via Monte Carlo simulation.

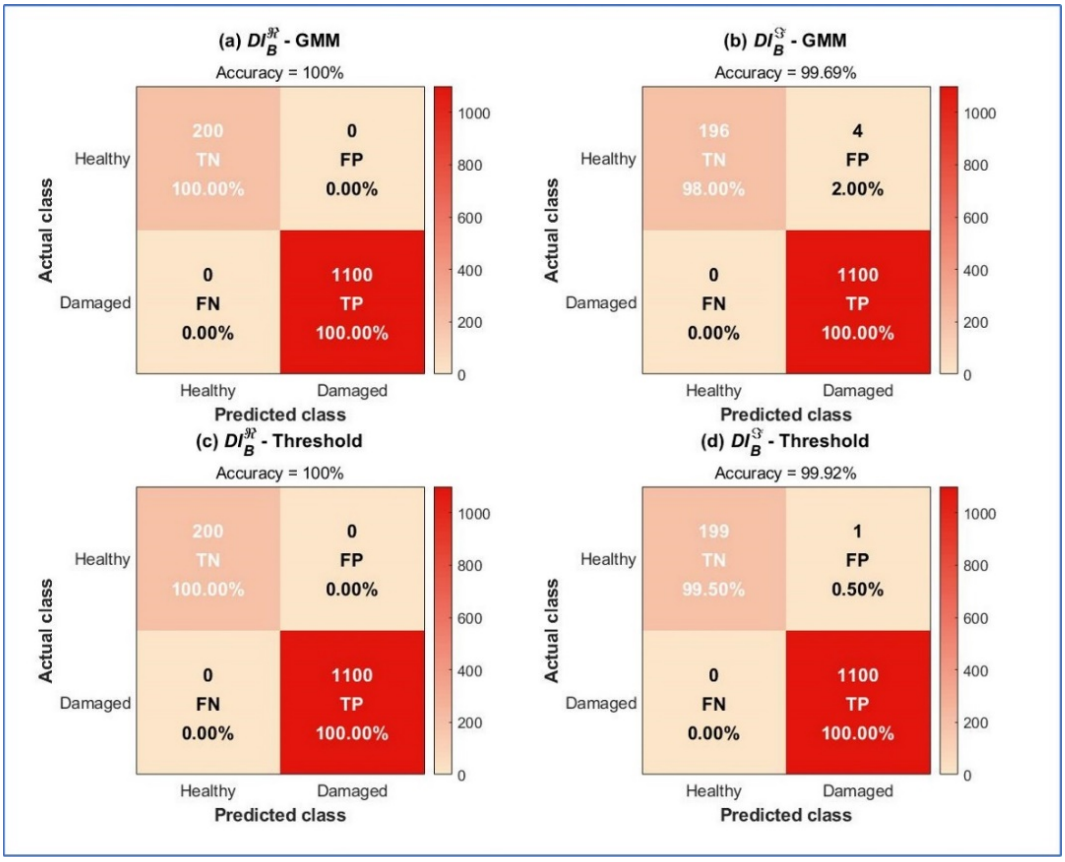

Figure 15. The confusion matrices of the novelty detection result of: (a) $DI_B^{\Re}$-GMM method; (b) $DI_B^{\Im}$-GMM method; (c) $DI_B^{\Re}$-threshold method; (d) $DI_B^{\Im}$-threshold method.

6. Conclusion

TF has been extensively adopted in SHM as a damage-sensitive and input-robust structural damage feature. However, current studies on TF normally cannot model and accommodate the uncertainties involved in novelty detection procedures. Therefore, it is reasonable to construct a TF-based damage indicator involving uncertainties to improve the performance and robustness of novelty detection. In this work, a novel damage indicator is proposed based on the probabilistic model of TFs using circularly-symmetric complex Gaussian ratio distribution and the Laplace approximation of D_B. The global maximum and Hessian matrix required in the Laplace asymptotic expansion are also derived analytically. In addition, a Bayesian resampling scheme is proposed to properly accommodate the variability of the estimation of statistical parameters involved in the probabilistic model of TFs. Two state discrimination approaches, including a GMM clustering method and a threshold method, are adopted to discriminate structural states based on the Bayesian resampling scheme.

Two case studies, including a laboratory application and a field test, are used to validate the novelty detection method. It can be found that the DI_B values deviate clearly from those of the baseline structure and hence indicates the occurrence of damage. Moreover, the DI_B values increase with the damage level, indicating that the approximated Bhattacharyya distance can reflect the relative damage extent. The first case study shows that the GMM-based method exhibits better performance and higher robustness in detecting the introduced nonlinearities than the threshold-based method. In the second case study, both the GMM-based method and the threshold-based method exhibit attractive performance, demonstrating the potential of these novelty detection methods for implementing on real civil structures. Compared to the MSD-threshold method, the proposed novelty detection method is more robust due to employing a more accurate statistical model of TFs and accommodating the uncertainties of the statistical parameters. However, damage localization and damage extent quantification are still not realized using the proposed novelty detection method. Therefore, these issues still need to be further investigated in the future.

Acknowledgments

This research has been supported by the Science and Technology Development Fund, Macau SAR (File no.: FDCT/017/2020/A1, FDCT/0101/2021/A2, FDCT/0010/2021/AGJ and SKL-

IOTSC(UM)-2021-2022), the Research Committee of University of Macau under Research Grant (File no.: MYRG2020-00073-IOTSC) and the Guangdong-Hong Kong-Macau Joint Laboratory Program (Project no.: 2020B1212030009). The authors highly appreciate VCE for sharing the field test data of S101 Bridge.

Appendix A: Optimal values of ${u_{ij}}^{k,\Re *}$ and ${u_{ij}}^{k,\Im *}$

The approximated Bhattacharyya distance is given by:

$$D_B{}^{\Re}\left(p\left({u_{ij}}^{k,\Re}\right), p^d\left({u_{ij}}^{k,\Re}\right)\right) = -\ln\left((2\pi)^{\frac{1}{2}}\, p_1\left({u_{ij}}^{k,\Re *}\right) p_2\left({u_{ij}}^{k,\Re *}\right)\left|H\left({u_{ij}}^{k,\Re *}\right)\right|^{-\frac{1}{2}}\right) \tag{A1}$$

The global maximum of the integrand, ${u_{ij}}^{k,\Re *}$, can be derived by solving the following equation:

$$p\left({u_{ij}}^{k,\Re}\right)\frac{\mathrm{d}p^d\left({u_{ij}}^{k,\Re}\right)}{\mathrm{d}{u_{ij}}^{k,\Re}} + p^d\left({u_{ij}}^{k,\Re}\right)\frac{\mathrm{d}p\left({u_{ij}}^{k,\Re}\right)}{\mathrm{d}{u_{ij}}^{k,\Re}} = 0 \tag{A2}$$

According to Eq. (5) and Eq. (7), the first derivatives of $p\left({u_{ij}}^{k,\Re}\right)$ and $p^d\left({u_{ij}}^{k,\Re}\right)$ can be calculated by Eq. (A3):

$$\begin{aligned}\frac{\mathrm{d}p\left({u_{ij}}^{k,\Re}\right)}{\mathrm{d}{u_{ij}}^{k,\Re}} = &-\frac{3}{4}\left(1-\left|{\rho_{ij}}^k\right|^2\right)\left({\sigma_j}^k\right)^4\left({\sigma_i}^k\right)^2\left(-2\left({\sigma_j}^k\right)^3{\sigma_i}^k{\rho_{ij}}^{k,\Re} + 2\left({\sigma_j}^k\right)^4{u_{ij}}^{k,\Re}\right)\times \\ &\left\{-2\left({\sigma_j}^k\right)^3{\sigma_i}^k{\rho_{ij}}^{k,\Re}{u_{ij}}^{k,\Re} + \left({\sigma_j}^k\right)^4\left({u_{ij}}^{k,\Re}\right)^2 + \left({\sigma_j}^k\right)^2\left({\sigma_i}^k\right)^2\left[1-\left({\rho_{ij}}^{k,\Im}\right)^2\right]\right\}^{-\frac{5}{2}}\end{aligned} \tag{A3a}$$

$$\begin{aligned}\frac{\mathrm{d}p^d\left({u_{ij}}^{k,\Re}\right)}{\mathrm{d}{u_{ij}}^{k,\Re}} = &-\frac{3}{4}\left(1-\left|{\tilde{\rho}_{ij}}^k\right|^2\right)\left({\tilde{\sigma}_j}^k\right)^4\left({\tilde{\sigma}_i}^k\right)^2\left(-2\left({\tilde{\sigma}_j}^k\right)^3{\tilde{\sigma}_i}^k{\tilde{\rho}_{ij}}^{k,\Re} + 2\left({\tilde{\sigma}_j}^k\right)^4{u_{ij}}^{k,\Re}\right)\times \\ &\left\{-2\left({\tilde{\sigma}_j}^k\right)^3{\tilde{\sigma}_i}^k{\tilde{\rho}_{ij}}^{k,\Re}{u_{ij}}^{k,\Re} + \left({\tilde{\sigma}_j}^k\right)^4\left({u_{ij}}^{k,\Re}\right)^2 + \left({\tilde{\sigma}_j}^k\right)^2\left({\tilde{\sigma}_i}^k\right)^2\left[1-\left({\tilde{\rho}_{ij}}^{k,\Im}\right)^2\right]\right\}^{-\frac{5}{2}}\end{aligned} \tag{A3b}$$

Therefore, Eq. (A2) can be rearranged as follows:

$$
\begin{aligned}
&\left(u_{ij}^{k,\Re}\right)^3 - \frac{3}{2}\left(\frac{\tilde{\sigma}_i^{k}\tilde{p}_{ij}^{k,\Re}}{\tilde{\sigma}_j^{k}} + \frac{\sigma_i^{k}\rho_{ij}^{k,\Re}}{\sigma_j^{k}}\right)\left(u_{ij}^{k,\Re}\right)^2 \\
&+\left[\frac{2\tilde{\sigma}_i^{k}\sigma_i^{k}\tilde{p}_{ij}^{k,\Re}\rho_{ij}^{k,\Re}}{\tilde{\sigma}_j^{k}\sigma_j^{k}} + \frac{\left(\tilde{\sigma}_i^{k}\right)^2\left(1-\left(\tilde{p}_{ij}^{k,\Im}\right)^2\right)}{2\left(\tilde{\sigma}_j^{k}\right)^2} + \frac{\left(\sigma_i^{k}\right)^2\left(1-\left(\rho_{ij}^{k,\Im}\right)^2\right)}{2\left(\sigma_j^{k}\right)^2}\right]u_{ij}^{k,\Re} \\
&-\left[\frac{\left(\sigma_i^{k}\right)^2\tilde{\sigma}_i^{k}\tilde{p}_{ij}^{k,\Re}\left(1-\left(\rho_{ij}^{k,\Im}\right)^2\right)}{2\left(\sigma_j^{k}\right)^2\tilde{\sigma}_j^{k}} + \frac{\left(\tilde{\sigma}_i^{k}\right)^2\sigma_i^{k}\rho_{ij}^{k,\Re}\left(1-\left(\tilde{p}_{ij}^{k,\Im}\right)^2\right)}{2\left(\tilde{\sigma}_j^{k}\right)^2\sigma_j^{k}}\right] = 0
\end{aligned}
\tag{A4}
$$

Eq. (A4) is a cubic equation in the form of $a\left(u_{ij}^{k,\Re}\right)^3 + b\left(u_{ij}^{k,\Re}\right)^2 + cu_{ij}^{k,\Re} + d = 0$ with $a = 1$, $b = -\frac{3}{2}\left(\frac{\tilde{\sigma}_i^{k}\tilde{p}_{ij}^{k,\Re}}{\tilde{\sigma}_j^{k}} + \frac{\sigma_i^{k}\rho_{ij}^{k,\Re}}{\sigma_j^{k}}\right)$, $c = \left[\frac{2\tilde{\sigma}_i^{k}\sigma_i^{k}\tilde{p}_{ij}^{k,\Re}\rho_{ij}^{k,\Re}}{\tilde{\sigma}_j^{k}\sigma_j^{k}} + \frac{\left(\tilde{\sigma}_i^{k}\right)^2\left(1-\left(\tilde{p}_{ij}^{k,\Im}\right)^2\right)}{2\left(\tilde{\sigma}_j^{k}\right)^2} + \frac{\left(\sigma_i^{k}\right)^2\left(1-\left(\rho_{ij}^{k,\Im}\right)^2\right)}{2\left(\sigma_j^{k}\right)^2}\right]$, and $d = -\left[\frac{\left(\sigma_i^{k}\right)^2\tilde{\sigma}_i^{k}\tilde{p}_{ij}^{k,\Re}\left(1-\left(\rho_{ij}^{k,\Im}\right)^2\right)}{2\left(\sigma_j^{k}\right)^2\tilde{\sigma}_j^{k}} + \frac{\left(\tilde{\sigma}_i^{k}\right)^2\sigma_i^{k}\rho_{ij}^{k,\Re}\left(1-\left(\tilde{p}_{ij}^{k,\Im}\right)^2\right)}{2\left(\tilde{\sigma}_j^{k}\right)^2\sigma_j^{k}}\right]$. Assume $u_{ij}^{k,\Re} = z - \frac{b}{3}$, then it has:

$$z^3 + pz + q = 0 \tag{A5}$$

where $p = c - \frac{b^2}{3}, q = \frac{2b^3}{27} - \frac{bc}{3} + d$. The discriminant of Eq. (A5) is denoted by:

$$\Delta = (\frac{q}{2})^2 + (\frac{p}{3})^3 \tag{A6}$$

For the complex correlation coefficient, it has $\left(\rho_{ij}^{k,\Re}\right)^2 + \left(\rho_{ij}^{k,\Im}\right)^2 < 1$. Therefore, the second derivative $\frac{\mathrm{d}^2\sqrt{p\left(u_{ij}^{k,\Re}\right)p^d\left(u_{ij}^{k,\Re}\right)}}{\mathrm{d}\left(u_{ij}^{k,\Re}\right)^2} < 0$. Since the premise of the Laplace approximation algorithm is the integrand has a single maximum over its domain $\mathbf{\Omega} \in \Re^n$, $\Delta > 0$ must be satisfied and thus Eq. (A5) has the only real root z^*, which is namely the single maximum for the function $f\left(z\right) = z^3 + pz + q$ over $\mathbf{\Omega}$ and can be calculated by:

$$z^{*}=\sqrt[3]{-\frac{q}{2}+\sqrt{\Delta}}+\sqrt[3]{-\frac{q}{2}-\sqrt{\Delta}} \tag{A7}$$

Then $u_{ij}^{k,\Re *}$ can be derived accordingly: $u_{ij}^{k,\Re *}=z^{*}-\frac{b}{3}$. Similarly, the optimal values of the imaginary part $u_{ij}^{k,\Im *}$ can also be derived in the same manner and the procedures are omitted here for the purpose of simplicity.

Appendix B: Hessian Matrix $H\left(u_{ij}^{k,\Re *}\right)$ and $H\left(u_{ij}^{k,\Im *}\right)$

Since $u_{ij}^{k,\Re}$ is a one-dimensional variable, the Hessian matrix can be estimated as:

$$H\left(u_{ij}^{k,\Re *}\right)=\left[\frac{\mathrm{d}^2\left(-\ln\left(p_1\left(u_{ij}^{k,\Re}\right)p_2\left(u_{ij}^{k,\Re}\right)\right)\right)}{\mathrm{d}\left(u_{ij}^{k,\Re}\right)^2}\right]_{u_{ij}^{k,\Re}=u_{ij}^{k,\Re *}} \tag{B1a}$$

$$\begin{aligned}\frac{\mathrm{d}^2\left[-\ln\left(p_1\left(u_{ij}^{k,\Re}\right)p_2\left(u_{ij}^{k,\Re}\right)\right)\right]}{\mathrm{d}\left(u_{ij}^{k,\Re}\right)^2}&=\frac{\mathrm{d}^2\left[-\ln p_1\left(u_{ij}^{k,\Re}\right)-\ln p_2\left(u_{ij}^{k,\Re}\right)\right]}{\mathrm{d}\left(u_{ij}^{k,\Re}\right)^2}\\&=-\frac{1}{2}\frac{\mathrm{d}^2\left[\ln p\left(u_{ij}^{k,\Re}\right)\right]}{\mathrm{d}\left(u_{ij}^{k,\Re}\right)^2}-\frac{1}{2}\frac{\mathrm{d}^2\left[\ln p^{d}\left(u_{ij}^{k,\Re}\right)\right]}{\mathrm{d}\left(u_{ij}^{k,\Re}\right)^2}\end{aligned} \tag{B1b}$$

The second derivatives can be solved analytically based on Eq. (5), Eq. (7) and Eq. (A3):

$$\begin{aligned}\frac{\mathrm{d}^2 p\left(u_{ij}^{k,\Re}\right)}{\mathrm{d}\left(u_{ij}^{k,\Re}\right)^2}=&\frac{15}{8}\left(1-\left|\rho_{ij}^{k}\right|^2\right)\left(\sigma_j^{k}\right)^4\left(\sigma_i^{k}\right)^2\left(-2\left(\sigma_j^{k}\right)^3\sigma_i^{k}\rho_{ij}^{k,\Re}+2\left(\sigma_j^{k}\right)^4u_{ij}^{k,\Re}\right)^2\times\\&\left\{-2\left(\sigma_j^{k}\right)^3\sigma_i^{k}\rho_{ij}^{k,\Re}u_{ij}^{k,\Re}+\left(\sigma_j^{k}\right)^4\left(u_{ij}^{k,\Re}\right)^2+\left(\sigma_j^{k}\right)^2\left(\sigma_i^{k}\right)^2\left[1-\left(\rho_{ij}^{k,\Im}\right)^2\right]\right\}^{-\frac{7}{2}}\\&-\frac{3}{2}\left(1-\left|\rho_{ij}^{k}\right|^2\right)\left(\sigma_j^{k}\right)^8\left(\sigma_i^{k}\right)^2\times\\&\left\{-2\left(\sigma_j^{k}\right)^3\sigma_i^{k}\rho_{ij}^{k,\Re}u_{ij}^{k,\Re}+\left(\sigma_j^{k}\right)^4\left(u_{ij}^{k,\Re}\right)^2+\left(\sigma_j^{k}\right)^2\left(\sigma_i^{k}\right)^2\left[1-\left(\rho_{ij}^{k,\Im}\right)^2\right]\right\}^{-\frac{5}{2}}\end{aligned} \tag{B2a}$$

$$\frac{\mathrm{d}^2 p^d\left(u_{ij}^{k,\Re}\right)}{\mathrm{d}\left(u_{ij}^{k,\Re}\right)^2}=\frac{15}{8}\left(\tilde{\sigma}_j^{\,k}\right)^4\left(\tilde{\sigma}_i^{\,k}\right)^2\left(-2\left(\tilde{\sigma}_j^{\,k}\right)^3\tilde{\sigma}_i^{\,k}\tilde{\rho}_{ij}^{\,k,\Re}+2\left(\tilde{\sigma}_j^{\,k}\right)^4u_{ij}^{\,k,\Re}\right)^2\times$$
$$\left\{-2\left(\tilde{\sigma}_j^{\,k}\right)^3\tilde{\sigma}_i^{\,k}\tilde{\rho}_{ij}^{\,k,\Re}u_{ij}^{\,k,\Re}+\left(\tilde{\sigma}_j^{\,k}\right)^4\left(u_{ij}^{\,k,\Re}\right)^2+\left(\tilde{\sigma}_j^{\,k}\right)^2\left(\tilde{\sigma}_i^{\,k}\right)^2\left[1-\left(\tilde{\rho}_{ij}^{\,k,\Im}\right)^2\right]\right\}^{-\frac{7}{2}}$$
$$-\frac{3}{2}\left(1-\left|\tilde{\rho}_{ij}^{\,k}\right|^2\right)\left(\tilde{\sigma}_j^{\,k}\right)^8\left(\tilde{\sigma}_i^{\,k}\right)^2\times$$
$$\left\{-2\left(\tilde{\sigma}_j^{\,k}\right)^3\tilde{\sigma}_i^{\,k}\tilde{\rho}_{ij}^{\,k,\Re}u_{ij}^{\,k,\Re}+\left(\tilde{\sigma}_j^{\,k}\right)^4\left(u_{ij}^{\,k,\Re}\right)^2+\left(\tilde{\sigma}_j^{\,k}\right)^2\left(\tilde{\sigma}_i^{\,k}\right)^2\left[1-\left(\tilde{\rho}_{ij}^{\,k,\Im}\right)^2\right]\right\}^{-\frac{5}{2}}\qquad\text{(B2b)}$$

$$\frac{\mathrm{d}^2\left[\ln p\left(u_{ij}^{k,\Re}\right)\right]}{\mathrm{d}\left(u_{ij}^{k,\Re}\right)^2}=\left[-\left(p\left(u_{ij}^{k,\Re}\right)\right)^{-2}\left(\frac{\mathrm{d}p\left(u_{ij}^{k,\Re}\right)}{\mathrm{d}u_{ij}^{k,\Re}}\right)^2+\left(p\left(u_{ij}^{k,\Re}\right)\right)^{-1}\frac{\mathrm{d}^2 p\left(u_{ij}^{k,\Re}\right)}{\mathrm{d}\left(u_{ij}^{k,\Re}\right)^2}\right]$$
$$=\frac{3}{2}\left(-2\left(\sigma_j^{\,k}\right)^3\sigma_i^{\,k}\rho_{ij}^{\,k,\Re}+2\left(\sigma_j^{\,k}\right)^4u_{ij}^{\,k,\Re}\right)^2\times$$
$$\left\{-2\left(\sigma_j^{\,k}\right)^3\sigma_i^{\,k}\rho_{ij}^{\,k,\Re}u_{ij}^{\,k,\Re}+\left(\sigma_j^{\,k}\right)^4\left(u_{ij}^{\,k,\Re}\right)^2+\left(\sigma_j^{\,k}\right)^2\left(\sigma_i^{\,k}\right)^2\left[1-\left(\rho_{ij}^{\,k,\Im}\right)^2\right]\right\}^{-2}\qquad\text{(B2c)}$$
$$-3\left(\sigma_j^{\,k}\right)^4\left\{-2\left(\sigma_j^{\,k}\right)^3\sigma_i^{\,k}\rho_{ij}^{\,k,\Re}u_{ij}^{\,k,\Re}+\left(\sigma_j^{\,k}\right)^4\left(u_{ij}^{\,k,\Re}\right)^2+\left(\sigma_j^{\,k}\right)^2\left(\sigma_i^{\,k}\right)^2\left[1-\left(\rho_{ij}^{\,k,\Im}\right)^2\right]\right\}^{-1}$$

$$\frac{\mathrm{d}^2\left[\ln p^d\left(u_{ij}^{k,\Re}\right)\right]}{\mathrm{d}\left(u_{ij}^{k,\Re}\right)^2}=\left[-\left(p^d\left(u_{ij}^{k,\Re}\right)\right)^{-2}\left(\frac{\mathrm{d}p^d\left(u_{ij}^{k,\Re}\right)}{\mathrm{d}u_{ij}^{k,\Re}}\right)^2+\left(p^d\left(u_{ij}^{k,\Re}\right)\right)^{-1}\frac{\mathrm{d}^2 p^d\left(u_{ij}^{k,\Re}\right)}{\mathrm{d}\left(u_{ij}^{k,\Re}\right)^2}\right]$$
$$=\frac{3}{2}\left(-2\left(\tilde{\sigma}_j^{\,k}\right)^3\tilde{\sigma}_i^{\,k}\tilde{\rho}_{ij}^{\,k,\Re}+2\left(\tilde{\sigma}_j^{\,k}\right)^4u_{ij}^{\,k,\Re}\right)^2\times$$
$$\left\{-2\left(\tilde{\sigma}_j^{\,k}\right)^3\tilde{\sigma}_i^{\,k}\tilde{\rho}_{ij}^{\,k,\Re}u_{ij}^{\,k,\Re}+\left(\tilde{\sigma}_j^{\,k}\right)^4\left(u_{ij}^{\,k,\Re}\right)^2+\left(\tilde{\sigma}_j^{\,k}\right)^2\left(\tilde{\sigma}_i^{\,k}\right)^2\left[1-\left(\tilde{\rho}_{ij}^{\,k,\Im}\right)^2\right]\right\}^{-2}\qquad\text{(B2d)}$$
$$-3\left(\tilde{\sigma}_j^{\,k}\right)^4\left\{-2\left(\tilde{\sigma}_j^{\,k}\right)^3\tilde{\sigma}_i^{\,k}\tilde{\rho}_{ij}^{\,k,\Re}u_{ij}^{\,k,\Re}+\left(\tilde{\sigma}_j^{\,k}\right)^4\left(u_{ij}^{\,k,\Re}\right)^2+\left(\tilde{\sigma}_j^{\,k}\right)^2\left(\tilde{\sigma}_i^{\,k}\right)^2\left[1-\left(\tilde{\rho}_{ij}^{\,k,\Im}\right)^2\right]\right\}^{-1}$$

Based on Eq. (A1)-Eq. (A7) and Eq. (B1)-Eq. (B2), the real part of D_B between TFs under two different states can be approximated using a Laplace asymptotic expansion method, which avoids direct numerical integration and thus significantly reduces computational cost and improves the efficiency. Similarly, the Laplace approximation for the imaginary part $D_B^{\Im}$ can also be derived analytically.

References:

1. Farrar, C.R. and K. Worden, *Structural health monitoring: a machine learning perspective*. 2012: John Wiley & Sons.
2. Mitra, M. and S. Gopalakrishnan, *Guided wave based structural health monitoring: A review.* Smart Materials and Structures, 2016. **25**(5): p. 053001.
3. Jiang, C., W. Li, M. Deng, and C.-T. Ng, *Quasistatic pulse generation of ultrasonic guided waves propagation in composites.* Journal of Sound and Vibration, 2022. **524**: p. 116764.
4. Yan, W.-J., D. Chronopoulos, C. Papadimitriou, S. Cantero-Chinchilla, and G.-S. Zhu, *Bayesian inference for damage identification based on analytical probabilistic model of scattering coefficient estimators and ultrafast wave scattering simulation scheme.* Journal of Sound and Vibration, 2020. **468**: p. 115083.
5. He, S. and C.-T. Ng, *Guided wave-based identification of multiple cracks in beams using a Bayesian approach.* Mechanical Systems and Signal Processing, 2017. **84**: p. 324-345.
6. Farrar, C.R., S.W. Doebling, and D.A. Nix, *Vibration–based structural damage identification.* Philosophical Transactions of the Royal Society of London. Series A: Mathematical, Physical and Engineering Sciences, 2001. **359**(1778): p. 131-149.
7. Yan, W.-J., D. Chronopoulos, K.-V. Yuen, and Y.-C. Zhu, *Structural anomaly detection based on probabilistic distance measures of transmissibility function and statistical threshold selection scheme.* Mechanical Systems and Signal Processing, 2022. **162**: p. 108009.
8. Chesné, S. and A. Deraemaeker, *Damage localization using transmissibility functions: a critical review.* Mechanical Systems and Signal Processing, 2013. **38**(2): p. 569-584.
9. Yan, W.-J., M.-Y. Zhao, Q. Sun, and W.-X. Ren, *Transmissibility-based system identification for structural health Monitoring: Fundamentals, approaches, and applications.* Mechanical Systems and Signal Processing, 2019. **117**: p. 453-482.
10. Maia, N.M., R.A. Almeida, A.P. Urgueira, and R.P. Sampaio, *Damage detection and quantification using transmissibility.* Mechanical Systems and Signal Processing, 2011. **25**(7): p. 2475-2483.
11. Chen, Q., Y. Chan, K. Worden, and G. Tomlinson. *Structural fault detection using neural networks trained on transmissibility functions*. in *Proceedings of the International Conference on Vibration Engineering*. 1994.
12. Zhang, H., M. Schulz, A. Naser, F. Ferguson, and P. Pai, *Structural health monitoring using transmittance functions.* Mechanical Systems and Signal Processing, 1999. **13**(5): p. 765-787.
13. Feng, L., X. Yi, D. Zhu, X. Xie, and Y. Wang, *Damage detection of metro tunnel structure through transmissibility function and cross correlation analysis using local excitation and measurement.* Mechanical Systems and Signal Processing, 2015. **60**: p. 59-74.
14. Zhao, X.Y., Z.-Q. Lang, G. Park, C.R. Farrar, M.D. Todd, Z. Mao, and K. Worden, *A new transmissibility analysis method for detection and location of damage via nonlinear features in MDOF structural systems.* IEEE/ASME transactions on mechatronics, 2014. **20**(4): p. 1933-1947.
15. Cheng, L. and A. Cigada, *An analytical perspective about structural damage identification based on transmissibility function.* Structural Health Monitoring, 2020. **19**(1): p. 142-155.
16. Worden, K. and G. Manson, *The application of machine learning to structural health monitoring.* Philosophical Transactions of the Royal Society A: Mathematical, Physical and Engineering Sciences, 2007. **365**(1851): p. 515-537.
17. Goi, Y. and C.-W. Kim, *Damage detection of a truss bridge utilizing a damage indicator from*

multivariate autoregressive model. Journal of Civil Structural Health Monitoring, 2017. **7**(2): p. 153-162.

18. Worden, K., *Structural fault detection using a novelty measure*. Journal of Sound and vibration, 1997. **201**(1): p. 85-101.
19. Worden, K., G. Manson, and N.R. Fieller, *Damage detection using outlier analysis*. Journal of Sound and Vibration, 2000. **229**(3): p. 647-667.
20. Worden, K., G. Manson, and D. Allman, *Experimental validation of a structural health monitoring methodology: Part I. Novelty detection on a laboratory structure*. Journal of Sound and Vibration, 2003. **259**(2): p. 323-343.
21. Figueiredo, E. and E. Cross, *Linear approaches to modeling nonlinearities in long-term monitoring of bridges*. Journal of Civil Structural Health Monitoring, 2013. **3**(3): p. 187-194.
22. Zhou, Y.-L., N.M. Maia, R.P. Sampaio, and M.A. Wahab, *Structural damage detection using transmissibility together with hierarchical clustering analysis and similarity measure*. Structural Health Monitoring, 2017. **16**(6): p. 711-731.
23. Mao, Z. and M. Todd, *A model for quantifying uncertainty in the estimation of noise-contaminated measurements of transmissibility*. Mechanical Systems and Signal Processing, 2012. **28**: p. 470-481.
24. Mao, Z. and M. Todd, *Rapid structural condition assessment using transmissibility with quantified confidence for decision making*, in *Topics in Model Validation and Uncertainty Quantification, Volume 4*. 2012, Springer. p. 133-140.
25. Poulimenos, A.G. and J.S. Sakellariou, *A transmittance-based methodology for damage detection under uncertainty: An application to a set of composite beams with manufacturing variability subject to impact damage and varying operating conditions*. Structural Health Monitoring, 2019. **18**(1): p. 318-333.
26. Yan, W.-J. and W.-X. Ren, *Circularly-symmetric complex normal ratio distribution for scalar transmissibility functions. Part I: Fundamentals*. Mechanical Systems and Signal Processing, 2016. **80**: p. 58-77.
27. Yan, W.-J. and W.-X. Ren, *Circularly-symmetric complex normal ratio distribution for scalar transmissibility functions. Part II: Probabilistic model and validation*. Mechanical Systems and Signal Processing, 2016. **80**: p. 78-98.
28. Choi, E. and C. Lee, *Feature extraction based on the Bhattacharyya distance*. Pattern Recognition, 2003. **36**(8): p. 1703-1709.
29. Xuan, G., P. Chai, and M. Wu. *Bhattacharyya distance feature selection*. in *Proceedings of 13th International Conference on Pattern Recognition*. 1996. IEEE.
30. Bhattacharyya, A., *On a measure of divergence between two statistical populations defined by their probability distributions*. Bull. Calcutta Math. Soc., 1943. **35**: p. 99-109.
31. Bi, S., M. Broggi, and M. Beer, *The role of the Bhattacharyya distance in stochastic model updating*. Mechanical Systems and Signal Processing, 2019. **117**: p. 437-452.
32. Bi, S., S. Prabhu, S. Cogan, and S. Atamturktur, *Uncertainty quantification metrics with varying statistical information in model calibration and validation*. AIAA journal, 2017. **55**(10): p. 3570-3583.
33. Yuen, K.-V. and L.S. Katafygiotis, *Bayesian fast Fourier transform approach for modal updating using ambient data*. Advances in Structural Engineering, 2003. **6**(2): p. 81-95.
34. Yuen, K.-V., L.S. Katafygiotis, and J.L. Beck, *Spectral density estimation of stochastic vector*

processes. Probabilistic Engineering Mechanics, 2002. **17**(3): p. 265-272.

35. Yan, W.-J. and W.-X. Ren, *Generalized proper complex gaussian ratio distribution and its application to statistical inference for frequency response functions.* Journal of Engineering Mechanics, 2018. **144**(9): p. 04018080.
36. Papadimitriou, C., J.L. Beck, and L.S. Katafygiotis, *Asymptotic expansions for reliability and moments of uncertain systems.* Journal of Engineering Mechanics, 1997. **123**(12): p. 1219-1229.
37. Beck, J.L. and K.-V. Yuen, *Model selection using response measurements: Bayesian probabilistic approach.* Journal of Engineering Mechanics, 2004. **130**(2): p. 192-203.
38. Au, S.-K., *Fast Bayesian FFT method for ambient modal identification with separated modes.* Journal of Engineering Mechanics, 2011. **137**(3): p. 214-226.
39. Rogers, T., K. Worden, R. Fuentes, N. Dervilis, U. Tygesen, and E. Cross, *A Bayesian non-parametric clustering approach for semi-supervised structural health monitoring.* Mechanical Systems and Signal Processing, 2019. **119**: p. 100-119.
40. Sarmadi, H., A. Entezami, M. Salar, and C. De Michele, *Bridge health monitoring in environmental variability by new clustering and threshold estimation methods.* Journal of Civil Structural Health Monitoring, 2021: p. 1-16.
41. Su, T. and J.G. Dy, *In search of deterministic methods for initializing K-means and Gaussian mixture clustering.* Intelligent Data Analysis, 2007. **11**(4): p. 319-338.
42. McLachlan, G.J. and D. Peel, *Finite mixture models*. 2004: John Wiley & Sons.
43. Figueiredo, E., G. Park, J. Figueiras, C. Farrar, and K. Worden, *Structural health monitoring algorithm comparisons using standard data sets*. 2009, Los Alamos National Lab.(LANL), Los Alamos, NM (United States).
44. Mousavi, M. and A.H. Gandomi, Structural health monitoring under environmental and operational variations using MCD prediction error. Journal of Sound and Vibration, 2021. 512: p.116370.
45. Figueiredo, E., G. Park, C.R. Farrar, K. Worden, and J. Figueiras, *Machine learning algorithms for damage detection under operational and environmental variability.* Structural Health Monitoring, 2011. **10**(6): p. 559-572.
46. Svendsen, B.T., O. Øiseth, G.T. Frøseth, and A. Rønnquist, *A hybrid structural health monitoring approach for damage detection in steel bridges under simulated environmental conditions using numerical and experimental data.* Structural Health Monitoring, 2022: p. 14759217221098998.
47. Bull, L., K. Worden, R. Fuentes, G. Manson, E. Cross, and N. Dervilis, *Outlier ensembles: A robust method for damage detection and unsupervised feature extraction from high-dimensional data.* Journal of Sound and Vibration, 2019. **453**: p. 126-150.
48. Sarmadi, H., A. Entezami, B. Behkamal, and C. De Michele, *Partially online damage detection using long-term modal data under severe environmental effects by unsupervised feature selection and local metric learning.* Journal of Civil Structural Health Monitoring, 2022: p. 1-24.
49. Sarmadi, H., A. Entezami, B. Saeedi Razavi, and K.V. Yuen, *Ensemble learning-based structural health monitoring by Mahalanobis distance metrics.* Structural Control and Health Monitoring, 2021. **28**(2): p. e2663.
50. Manson, G., K. Worden, and D. Allman, *Experimental validation of a structural health monitoring methodology: Part II. Novelty detection on a Gnat aircraft.* Journal of Sound and

Vibration, 2003. **259**(2): p. 345-363.

51. Engineers, V.C., *Progressive damage test S101. Flyover Reibersdorf.* Rep. No. 08, 2009. **2308**.

52. Döhler, M., F. Hille, L. Mevel, and W. Rücker, *Structural health monitoring with statistical methods during progressive damage test of S101 Bridge.* Engineering Structures, 2014. **69**: p. 183-193.